



# The detailed nature of active central cluster galaxies

S. I. Loubser<sup>1</sup>\* and I. K. Soechting<sup>2</sup>

<sup>1</sup>Centre for Space Research, North-West University, Potchefstroom 2520, South Africa

<sup>2</sup>Astrophysics, Department of Physics, University of Oxford, Oxford OX1 3RH, UK

Accepted 2013 March 1. Received 2013 February 25; in original form 2012 September 7

## ABSTRACT

We present detailed integral field unit observations of the central few kiloparsecs of the ionized nebulae surrounding four active central cluster galaxies (CCGs) in cooling flow clusters (Abell 0496, 0780, 1644 and 2052). Our sample consists of CCGs with H $\alpha$  filaments, and have existing data from the X-ray regime available. Here, we present the detailed optical emission-line (and simultaneous absorption line) data over a broad wavelength range to probe the dominant ionization processes, excitation sources, morphology and kinematics of the hot gas (as well as the morphology and kinematics of the stars). This, combined with the other multiwavelength data, will form a complete view of the different phases (hot and cold gas and stars) and how they interact in the processes of star formation and feedback detected in central galaxies in cooling flow clusters, as well as the influence of the host cluster. We derive the optical dust extinction maps of the four nebulae. We also derive a range of different kinematic properties, given the small sample size. For Abell 0496 and 0780, we find that the stars and gas are kinematically decoupled, and in the case of Abell 1644 we find that these components are aligned. For Abell 2052, we find that the gaseous components show rotation even though no rotation is apparent in the stellar components. To the degree that our spatial resolution reveals, it appears that all the optical forbidden and hydrogen recombination lines originate in the same gas for all the galaxies. Based on optical diagnostic ratios ([O III]  $\lambda$ 5007/H $\beta$  against [N II]  $\lambda$ 6584/H $\alpha$ , [S II]  $\lambda\lambda$ 6717, 6731/H $\alpha$  and [O I]  $\lambda$ 6300/H $\alpha$ ), all galaxies show extended low-ionization nuclear emission-line region emission, but that at least one has significant Seyfert emission areas, and at least one other has significant H II-like emission line ratios for many pixels. We also show that the hardness of the ionizing continuum do not decrease with galactocentric distance within our field-of-view (with the exception of one galaxy that show a core separation) as the emission line ratios do not vary significantly with radius. This also indicates that the derived nebular properties are spatially homogeneous. We fit active galactic nucleus (AGN) and post-asymptotic giant branch (pAGB) stars photoionization models as well as shock excitation models to our derived diagnostic ratios. These fits, combined with information from multiwavelength studies, reveal that AGN photoionization is the most likely ionization mechanism in at least two cases even though shocks and pAGB stars cannot be conclusively eliminated.

**Key words:** galaxies: clusters: individual: Abell 0496 – galaxies: clusters: individual: Abell 0780 – galaxies: clusters: individual: Abell 1644 – galaxies: clusters: individual: Abell 2052 – galaxies: elliptical and lenticular, cD – galaxies: formation.

## 1 INTRODUCTION

Decades ago, elliptical galaxies were thought to contain very little, if any, gas. Studies of galaxy formation, therefore, often focused on the stellar properties; however, we now know that a large fraction of the baryonic mass in massive galaxies is believed to be in

diffuse form. Thus a complete view of galaxy formation and evolution necessarily incorporates both the stars and hot gas and an understanding of the processes by which these phases interact (McCarthy et al. 2010).

Cooling-flow clusters are common in the local Universe and massive central cluster galaxies (CCGs) are often found at the centres of these systems (Peres et al. 1998). If the central cluster density is high enough, intracluster gas can condense and form stars at the bottom of the potential well. Since the radiative cooling times for

\* E-mail: ilani.loubser@nw.ac.za

intracluster gas are short enough that gas can cool and settle to the cluster centre (Edge, Stewart & Fabian 1992), it has been suggested that the big envelopes of CCGs may arise from the gradual deposition of this cool gas. More recently, high spectral resolution *XMM-Newton* observations showed that the X-ray gas in cluster centres does not cool significantly below a threshold temperature of  $kT \sim 1\text{--}2$  keV (Jordán et al. 2004, and references therein). This initially contradicted the model that these young stars are formed in cooling flows. However, it is possible that star formation is ongoing in cool-core clusters at a much reduced rate (Bildfell et al. 2008).

Previous studies have reported several examples of ongoing star formation in CCGs, in particular those hosted by cooling-flow clusters (Cardiel, Gorgas & Aragón-Salamanca 1998; Crawford et al. 1999; McNamara et al. 2006; Edwards et al. 2007; Bildfell et al. 2008; O'Dea et al. 2008; Loubser et al. 2009; Pipino et al. 2009). However, the origin of the gas fuelling this star formation is not yet known. Possible explanations include processes involving cooling flows or cold gas deposited during a merging event (Bildfell et al. 2008). These processes will leave different imprints in the dynamical properties, the detailed chemical abundances and the star formation histories of these galaxies, which can be studied using high-quality spectroscopy (Loubser et al. 2008, 2009; Loubser & Sánchez-Blázquez 2012).

Observations that support this idea are blue- and ultraviolet-colour (UV-colour) excesses observed (indicative of star formation) in the central galaxy of Abell 1795 by McNamara et al. (1996) and molecular gas detected in 10 out of 32 CCGs by Salomé & Combes (2003). The observations by Cardiel et al. (1998) were consistent with an evolutionary sequence in which star formation bursts, triggered by radio sources, take place several times during the lifetime of the cooling flow in the centre of the cluster. However, McNamara & O'Connell (1992) found only colour anomalies with small amplitudes, implying star formation rates that account for at most a few per cent of the material that is cooling and accreting on to the central galaxy. Cooling-flow models for CCG formation also imply the formation of larger numbers of new stars, for which there is no good observational evidence (Athanasoula, Garijo & García-Gómez 2001). The CCGs often host radio-loud active galactic nucleus (AGN) which may account for the necessary heating to counteract radiative cooling (Von der Linden et al. 2007).

In summary, cooling flow models predict more cooled gas than is observed (Bohringer et al. 2001). Thus, it is possible that the mass deposited into the molecular clouds is heated by one of several processes – hot young stellar populations, radio-loud AGN, X-rays or heat conduction from the intracluster medium (ICM) itself, shocks and turbulent mixing layers and cosmic rays. Therefore, only a small fraction of the cooled gas is detected (Crawford et al. 2005; Ferland et al. 2009). Thus, CCGs lie at the interface where it is crucial to understand the role of feedback and accretion in star formation. Within these cooling-flow CCGs, cool molecular clouds, warm ionized hydrogen and the cooling ICM are related. A complete view of the star formation process incorporates the stars with the gas and an understanding of the processes by which these phases interact, and therefore, requires information from several wavelength regimes.

In conclusion, although CCGs are probably not completely formed in cooling flows, the flows play an important role in regulating the rate at which gas cools at the centres of groups and clusters. In the  $\Lambda$  cold dark matter ( $\Lambda$ CDM) cosmology it is now understood that local massive haloes assemble late through the merging of smaller systems. In this picture, cooling flows seem to be the main fuel for galaxy mass growth at high redshift. This source is

removed only at low redshifts in group or cluster environments, due to AGN feedback (De Lucia & Blaizot 2007; Voit et al. 2008). Indeed, if AGN feedback is not properly assumed in hydrodynamical simulations, an apparently bluer brightest cluster galaxy (BCG) is formed as a result of an accelerated late stellar birthrate even after the epoch of quiescent star formation (Romeo et al. 2008).

We proposed and obtained integral field unit (IFU) observations of the central few kiloparsecs of the ionized nebulae in active CCGs in cooling-flow clusters. These observations will map the morphology, kinematics and ionization state of the nebulae to gain an understanding of their formation, heating and relationship to the cluster centre. We selected galaxies from the McDonald et al. (2010) study, which consisted of an  $H\alpha$  survey of 23 cooling flow clusters. Amongst their conclusions, McDonald, Veilleux & Rupke (2012) find a strong correlation between the  $H\alpha$  luminosity contained in filaments and the X-ray cooling flow rate of the cluster, suggesting that the warm, ionized gas is linked to the cooling flow. We chose objects with confirmed extended  $H\alpha$  emission, and with near-IR [Two Micron All Sky Survey (2MASS)], ultraviolet [*Galaxy Evolution Explorer (GALEX)*], X-ray data (*Chandra*) and in some cases Very Large Array (VLA) 1.4 GHz fluxes, already available (McDonald et al. 2010). Detailed properties of the host clusters, which are reported to influence the activity in the central galaxy, such as central cooling times and the offset between the cluster X-ray peak and the central galaxy, have been derived.

Farage et al. (2010) presented IFU observations of one nearby BCG showing low-ionization nuclear emission-line region (LINER)-like emission, and Brough et al. (2011) presented IFU data on four CCGs at  $z \sim 0.1$  to calculate the dynamical masses of CCGs and measure their stellar angular momentum (although none of their four CCGs contained emission lines). The Spectrographic Areal Unit for Research on Optical Nebulae (SAURON) sample includes only one CCG (M87). Hatch, Crawford & Fabian (2007) and Edwards et al. (2009) analysed data comparable to the data presented here. Hatch et al. (2007) present IFU observations of six emission-line nebulae in cool-core clusters (selected from the optical *ROSAT* follow-up by Crawford et al. 1999) with OASIS on the William Herschel Telescope (WHT; with a limited wavelength range centred around  $H\alpha$ ). Edwards et al. (2009) present IFU observations of nine CCGs in cooling and non-cooling clusters (also from Crawford et al. 1999) and within 50 kpc of the X-ray centre, with Gemini Multi-Object Spectrograph (GMOS) IFU and OASIS on WHT (most galaxies with wavelength ranges also limited to the  $H\alpha$  region, but three also included  $H\beta$ ). Emission line maps of morphology, kinematics, often line ratios, and the stellar continuum have been published for Abell 496 by Hatch et al. (2007), and for Abell 2052 by Edwards et al. (2009). These studies concluded that no proposed heating mechanism reproduces all the emission-line properties within their observed wavelength within a single source. Thus, a single dominant mechanism may not apply to all CCG nebulae, and there may be a mixture of heating mechanisms acting within a single nebula (Wilman, Edge & Swinbank 2006; Hatch et al. 2007). Thus to get more information which will enable the dominant mechanism(s) to be identified, we observed more line ratios over a longer wavelength range (around  $H\alpha$  and  $H\beta$  which also allowed extinction to be appropriately measured). We will be adding the detailed stellar population analysis, and place the derived information from the optical spectra in context with multiwavelength data over the full spectrum in a future paper, to explain the diverse nature of these galaxies. All the data for Abell 780 and 1644 are new, and all four of the extinction maps are new. Also, the construction of ionization diagrams and analysis of ionization processes with

**Table 1.** Galaxies observed with the Gemini South telescope. All four galaxies show extended H $\alpha$  emission (McDonald et al. 2010). The cluster X-ray temperature ( $T_X$ ) and classical cooling rates ( $\dot{M}$ ) are from White et al. (1997). The spectrally determined cooling rates are from McDonald et al. (2010). The values for  $R_{\text{off}}$  are from Edwards et al. (2007), with the exception of PGC 044257 which is from Peres et al. (1998).

Object	Cluster	Redshift $z$	Linear scale (kpc arcsec $^{-1}$ )	$R_{\text{off}}$ (Mpc)	$T_X$ (keV)	Classical cooling rates ( $M_{\odot} \text{ yr}^{-2}$ )	Spectrally determined ( $M_{\odot} \text{ yr}^{-2}$ )	Exposure time (s)
MCG-02-12-039	Abell 0496	0.0329	0.654	0.031	4.8	134	1.5	$7 \times 1800$
PGC 026269	Abell 0780	0.0539	1.059	0.015	4.7	222	7.5	$6 \times 1800$
PGC 044257	Abell 1644	0.0474	0.935	0.009	5.1	12	3.2	$6 \times 1800$
UGC 09799	Abell 2052	0.0345	0.685	0.038	3.4	94	2.6	$6 \times 1800$

shock models and post-asymptotic giant branch (pAGB) models are also new. Our exposure times (improved from previous studies) are shown in Table 1. These data are also complimentary to the long-slit spectroscopy (on Keck and Magellan) along the H $\alpha$  filaments of the four objects (studied here) by McDonald et al. (2012).

We introduce the sample and detail of the data reductions in Sections 2 and 3. We then derive the optical extinction as well as the line strengths in Section 4. We proceed to discuss the four individual cases in Section 5, and identify the mechanism producing the emission and the ionized gas in these four CCGs in Section 6. We summarize the findings of this paper in Section 7. We have used the following set of cosmological parameters:  $\Omega_m = 0.3$ ,  $\Omega_\Lambda = 0.7$ ,  $H_0 = 70 \text{ km s}^{-1} \text{ Mpc}^{-1}$ .

## 2 SAMPLE

We have chosen our sample of active CCGs from the H $\alpha$  imaging presented in McDonald et al. (2010), who in turn, selected their sample from White, Jones & Forman (1997). McDonald et al. (2010) enforced the cuts:  $\delta < +35^\circ$  and  $0.025 < z < 0.092$ , after which they selected 23 clusters to cover the full range of properties, from very rich clusters with high cooling rates to low-density clusters with small cooling flows. Their classical cooling rates range from 6.3 to  $431 M_{\odot} \text{ yr}^{-1}$  which means that while covering a large range in properties, their sample consisted of only cooling flow clusters. From their 23 cooling flow clusters, we selected all the clusters with clearly detected H $\alpha$  in their centres (albeit filamentary, extended or nuclear emission). In addition, all of these central galaxies have optical imaging, near-IR (2MASS) and UV (*GALEX* data) available. Thereafter, we selected all the central galaxies with detailed X-ray (*Chandra*) data, as well as VLA 1.4 GHz fluxes, available. This resulted in a subsample of 10 galaxies. We observed four of these galaxies with the GMOS IFU (as shown in Fig. 1). We merely chose the objects with the most auxiliary information available. This additional information will be added in the future paper (where the underlying stellar populations will be analysed in detail) and might help to constrain the ionization mechanisms.

The rest-wavelength range of the emission lines of interest is 4860–6731 Å (H $\beta$  to [S II]  $\lambda 6731$ ). The ratio of the forbidden [N II]  $\lambda 6584$  to H $\alpha$  line will depend on the metallicity of the gas, the form of the ionizing radiation and the star formation rate. The relative strength of the [O III]  $\lambda 5007$  and H $\beta$  lines reveals further excitation mechanism and gas metallicity information. The role of AGN photoionization is confined to the central 2–3 arcsec of active, massive nearby elliptical galaxies (Sarzi et al. 2006). Thus, IFU observations are ideal and will also allow us to study the 2D distribution of the ionizing radiation. In addition to the information from the emission lines, we are able to extract the underlying stellar absorption spectra using the improved GANDALF code (Sarzi et al. 2006). Thus, the kinematics and morphology of the hot ionized gas and stellar components can be correlated.

## 3 OBSERVATIONS AND DATA REDUCTION

The data were obtained with the GMOS IFU on the Gemini South telescope in semester 2011A (2011 February to July). The GMOS-IFU in one-slit mode was used and allowed us to map at least a 3 kpc wide region in the centre of the target galaxies with a simultaneous coverage of the 4600–6800 Å range in the target rest frame (using the B600 grating) with a single pointing. This resulted in a spectral resolution of 1.5 Å. This spectral resolution ( $81 \text{ km s}^{-1}$ ) is poorer than that of Edwards et al. (2007, who had a much shorter wavelength range), and much higher than that of Hatch et al. (2007) ( $223$ – $273 \text{ km s}^{-1}$ ).

The IFU field-of-view (FOV) is  $5 \times 3.5 \text{ arcsec}^2$ , and this area is divided into 500 lenslets (and another 250 lenslets offset for sky measurements). We obtained six exposures per galaxy, with the exception of MCG-02-12-039 where we obtained seven exposures, resulting in a total of 12 500 galaxy spectra. The targets, exposure times and other properties are shown in Tables 1 and 2. Our integration time is three times that of Edwards et al. (2009), and more than five times that of Hatch et al. (2007) with a much bigger instrument. In addition to the targets, the necessary bias, flat-fields, twilight flat-fields and arcs frames at two different central wavelengths were also observed, as well as a spectrophotometric standard star for flux calibration. Two central wavelength settings were used to avoid losing crucial spectral information in the two CCD gaps.

For more detail on the GMOS IFU data reduction process see Gerssen et al. (2006). The basic data reduction was done using the GMOS package in IRAF. The IFU sky-to-detector mapping was stored in the data array prior to data reduction. Several bias frames were averaged and subtracted directly from raw data, to correct the zero-point for each pixel. Additional care was taken to avoid including raw bias frames in the mean bias frame that drifted measurably with time. Frames were mosaicked, and the overscan regions were trimmed. Flat-field and twilight flat-field frames were used to correct for differences in sensitivity both between detector pixels and across the IFU field. The majority of the cosmic rays were rejected in the individual frames before sky subtraction using the Gemini cosmic ray rejection routine. The remainder of the cosmic rays were eliminated using the LACOSMIC routine (van Dokkum 2001) with an IRAF script that retained the multi-extension FITS format for further reductions. The sets of 2D spectra were calibrated in wavelength using the arc lamp spectra for the two different central wavelength settings. The IFU elements were, thereafter, extracted from the raw data format to a format more convenient for further processing. Sky emission lines and continuum were removed by averaging the sky spectrum over a number of spatial pixels (from the offset sky fibres on the edge of the science field) to reduce the noise level, before subtracting it from all the spatial pixels. Thus the process adds little extra noise to the result since the observations were obtained in dark time (the variability of the sky region was minimal), and a number of 250 spaxels were averaged in the sky-subtraction process. Thus, the

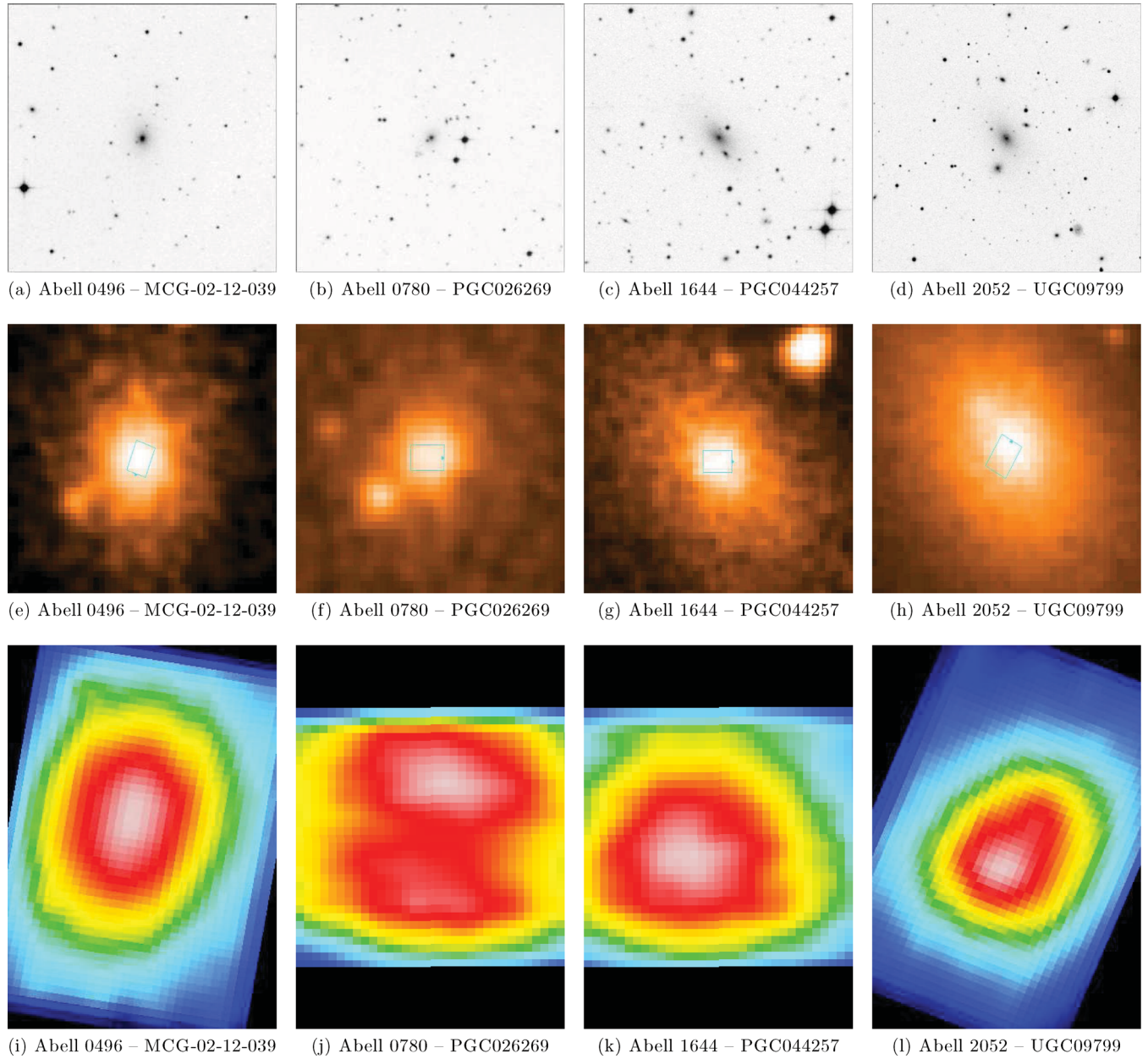


**Figure 1.** Digitized Sky Survey (DSS) images of the four targets (north above, and east to the left for all images). The upper plots show  $8 \times 8$  arcmin $^2$  FOVs, and the middle plots show the targets with the  $5 \times 3.5$  arcsec $^2$  IFU FOV overlaid. The top of the IFU FOV is indicated with a blue arrow. The lower plots show continuum images made from the IFU cubes (width of 50 at 6350 Å), smoothed spatially with a Gaussian with width 3 spaxels (which corresponds to 0.3 arcsec) and using the SAURON colour map.

**Table 2.** Further properties of the CCGs observed on Gemini South. Radio fluxes are from the NRAO VLA Sky Survey (NVSS).

Object	Cluster	Rest wavelength range (Å)	Foreground extinction (mag) $E(B - V)_{\text{galactic}}$	Average extinction (mag) measured $E(B - V)_{\text{total}}$	Radio flux (mJy)
MCG-02-12-039	Abell 0496	4648–7540	0.140	0.425	121
PGC 026269	Abell 0780	4743–7693	0.042	0.210	40 800
PGC 044257	Abell 1644	4713–7646	0.071	0.195	98
UGC 09799	Abell 2051	4655–7552	0.037	0.460	5500

error contribution of the sky-subtraction process is  $\frac{1}{\sqrt{250}} \times$  the error on one sky spaxel. A spectrophotometric standard star (LTT 4816) was used to correct the measured counts for the combined transmission of the instrument, telescope and atmosphere as a function of

wavelength. We reduced the standard star observation with the same instrument configuration as the corresponding scientific data. A 1D spectrum was extracted by adding the central spatial pixels from the standard star observation, and it was used to convert the measured

**Table 3.** Properties of the underlying stellar populations.

Object	Spectral types in the global optimal template
MCG-02-12-039	A0 Ia, G0, G1 Ib, G5, G8 III, K0, K0 III, K IIvw
PGC 026269	A0 Ia, K0 Ibvar, M4 III
PGC 044257	B3 III, A5, F3 V, F6, F7 V, G0 Vw, G1 Ib, G5, G5 V, G8 III/IVw, K1 III
UGC 09799	B8 Ib, A5, F3 III, G0 Vw, G1 Ib, K0 III

counts from the galaxy spectra into fluxes with  $\text{erg cm}^{-2} \text{s}^{-1} \text{\AA}^{-1}$  units.

The reduced 2D arrays were transformed back to a physical coordinate grid ( $x, y, \lambda$  data cube) before scientific analysis, while also correcting for atmospheric dispersion. The latter (also called differential refraction) causes the position of a target within the IFU field to vary with wavelength. This correction was necessary as data were taken at different airmasses throughout the observing nights. The spatial offset as a function of wavelength was determined using an atmospheric refraction model (given the airmass, position angle and other parameters) from the SLALIB positional astronomy library. Each hexagonal spaxel (each spatial element) was 0.2 arcsec, and this was subsampled on to a rectangular grid of 0.1 arcsec spaxel $^{-1}$  when the separate exposures were combined. The exposures were combined (median averaged) using a centroid algorithm to calculate the shifting in  $x$  and  $y$ , and also shifting in  $\lambda$  for the exposures at two different wavelength settings. No additional cosmic rays were visible after the LACOSMIC task was run on the individual cubes, so cosmic rays were not removed during this step. The cubes were also converted into row-stacked spectra (RSS) for further data reductions in IDL. Each spaxel was averaged with its eight neighbouring spaxels [improving the signal-to-noise ratio (S/N) by a factor of 3], which is effectively smoothing over 0.3 arcsec – this is still slightly undersampled compared to the average seeing ( $\sim 1$  arcsec), but only larger regions will be analysed further.

#### 4 LINE MEASUREMENTS AND INTERNAL EXTINCTION

To accurately measure the emission-line fluxes of the CCG spectra, we use a combination of the ppxf (Cappellari & Emsellem 2004) and Gas and Absorption Line Fitting (GANDALF) algorithm (Sarzi et al. 2006) routines.<sup>1</sup> GANDALF version 1.5 was used as it enables a reddening correction to be performed, and it incorporates errors. This code treats the emission lines as additional Gaussian templates, and solves linearly at each step for their amplitudes and the optimal combination of stellar templates, which are convolved by the best stellar line-of-sight velocity distribution. The stellar continuum and emission lines are fitted simultaneously. All 985 stars of the MILES stellar library (Sánchez-Blázquez et al. 2006) were used as stellar templates to automatically include  $\alpha$ -enhancement in the derived optimal template. The emission lines were masked while the optimal template was derived. The H $\alpha$  and [N II]  $\lambda\lambda 6583$  lines were fitted first, and the kinematics of all the other lines were tied to these lines, following the procedure described in Sarzi et al. (2006). However, in cases where the emission of the other lines were strong enough to measure velocity and velocity dispersion (as was mainly the case except for the extreme edges of the data cube), this was calculated independently as there is no a priori reason to expect the kinematics measured from all the lines to be the same (as they can originate in

different regions). After the kinematics are fixed, a Gaussian template is constructed for each emission line at each iteration, and the best linear combination of both stellar and emission-line templates (with positive weights) is determined. This is done without assuming line ratios, except in the case of doublets where their relative strength is fixed by the ratio of the corresponding transition probabilities. We have adapted the GANDALF code to apply it to the GMOS IFU cubes for a longer wavelength range. All 1617 spaxels were collapsed together to obtain a 1D spectrum per cube, thereafter all 985 stars for the MILES library were used to create a global optimal template for each galaxy. This global optimal template (and the stars it consisted of – to account for varying weights over the spatial region) was then applied to all 1617 spectra per cube. The spectral types of the stars that the global optimal templates consisted of (from the MILES library) are shown in Table 3.

Some ellipticals contain dust in the centre that can be patchy, uniform or filamentary (Laine et al. 2003). The long wavelength range of the spectra allows us to constrain the amount of reddening using the observed decrement of the Balmer lines, which can be set to have an intrinsic decrement consistent with the recombination theory by treating the lines as a multiplet. The physical constraints on the emission from the higher order Balmer lines also ensures the strength of the corresponding absorption features is correctly estimated.

We used the dust models by Calzetti et al. (2000) to calculate the flux attenuation values at the desired wavelength for any given  $E(B - V)$  value (optional see below). The Balmer decrement assumes a case B recombination for a density of  $100 \text{ cm}^{-3}$  and a temperature of  $10^4 \text{ K}$ , resulting in the predicted H $\alpha$ /H $\beta$  ratio of 2.86 (Osterbrock 1989). The code can adopt either a single dust component, affecting both the stellar continuum and the emission-line fluxes, or in addition include a second dust component that affects only the emission-line templates. We did not specify Galactic extinction [from the NASA/IPAC Extragalactic Database (NED); Schlegel, Finkbeiner & Davis 1998], but we measured a total diffuse component which gave the total extinction (hence including the foreground galactic extinction). This total extinction measured from the Balmer decrement is shown in Fig. 2 and averages are noted in Table 2 (the galactic extinction noted in Table 2 was not subtracted). The extinction was smoothed over 0.3 arcsec, and is only plotted where the velocity dispersion of the H $\alpha$  line is less than 500 km s $^{-1}$  (to avoid spaxels where the H $\alpha$  line could not be separated from the [N II] lines), and it is only plotted where the amplitude-to-noise ratio (A/N) of the H $\alpha$  line is higher than 3 (as defined in Sarzi et al. 2006).<sup>2</sup> The A/N maps of the H $\alpha$  measurements are shown in Section 5 which gives a direct indication of the errors on the extinction.

The parameter  $E(B - V)$ , i.e. the colour excess between 4350 and 5550 Å, for the galactic extinction for each of the four galaxies was taken from the NED data base (Schlegel et al. 1998), and ranged

<sup>1</sup> We make use of the corresponding ppxf and GANDALF IDL codes which can be retrieved at <http://www.leidenuniv.nl/sauron/>

<sup>2</sup> The A/N is related to the S/N:  $\text{EW} = \frac{F}{S} = \frac{\text{A/N} \sqrt{2\pi}\sigma}{\text{S/N}}$ , where EW is the equivalent width of the line, and  $\sigma$  is the line width.

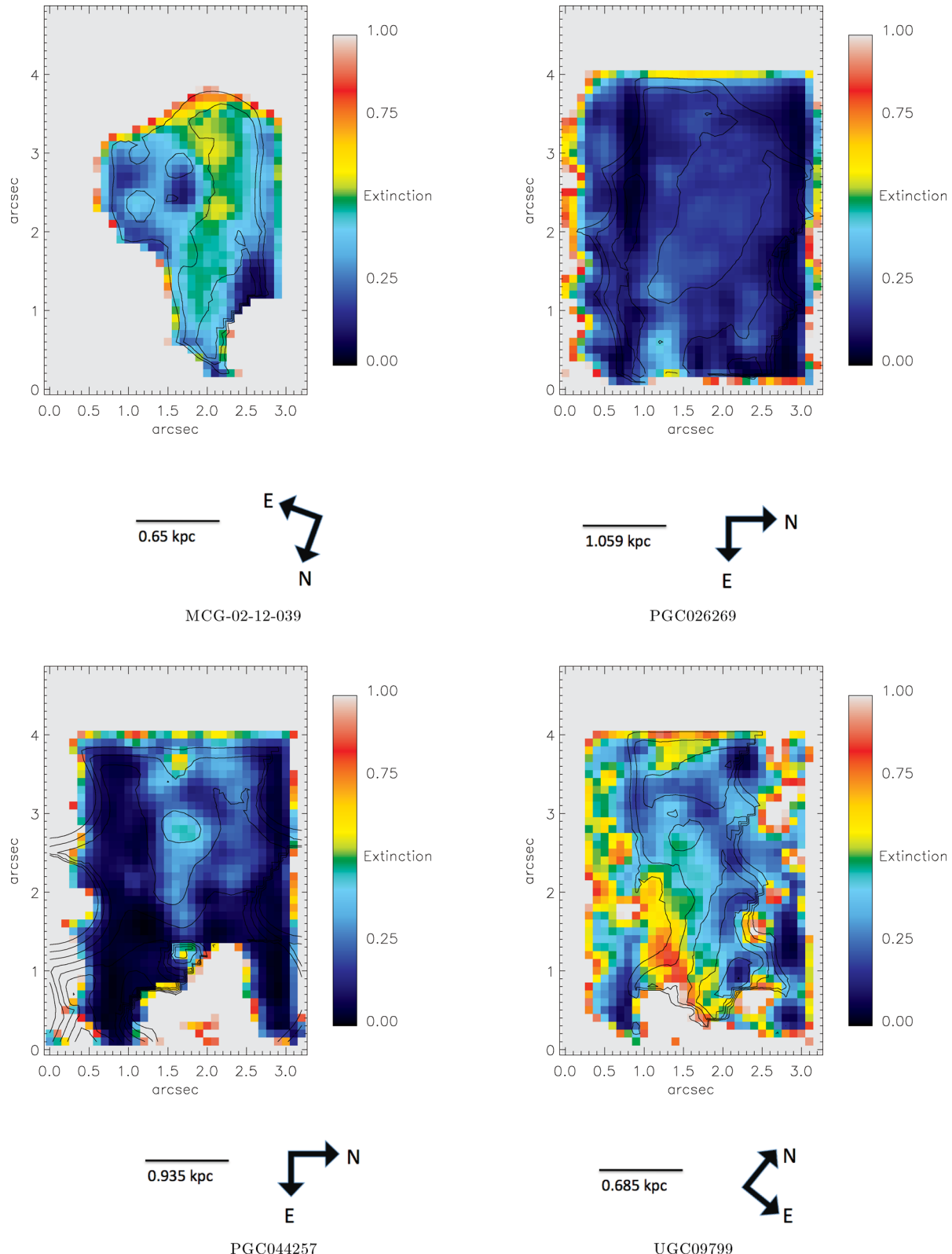


**Figure 2.** Total extinction of the four CCGs. The extinction was smoothed over 0.3 arcsec, and is only plotted where the velocity dispersion of the H $\alpha$  line is less than 500 km s $^{-1}$  (to avoid spaxels where the H $\alpha$  line could not be separated from the [N II] lines), and it is only plotted where the A/N of the H $\alpha$  line is higher than 3. Overplotted is the H $\alpha$  flux contours 1 mag apart. The grey regions in these, and all other, IFU maps are where the A/N is too low to plot.

between 0.037 and 0.140 mag (Table 2). The parameter  $R_V$ , i.e. the ratio of the absolute extinction at 5550 Å ( $A_V$ ) to the colour excess  $E(B - V)$ , was taken as 3.1 for the interstellar medium (Cardelli, Clayton & Mathis 1989). The total extinction is given by

$$E(B - V)_{\text{total}} = \frac{2.177}{-0.37R_V} \left( \log \frac{H\alpha_0}{H\beta_0} - \log \frac{H\alpha_{\text{Obs}}}{H\beta_{\text{Obs}}} \right).$$

The theoretical H $\alpha$ /H $\beta$  flux ratio of 2.86 may not be the ideal value to use for Seyfert-type galaxies, but the actual value is debated. It is often assumed that the H $\alpha$  emission in these systems is enhanced due to collisional processes, and several authors use a value  $R_V$  of 3.1 (Gaskell & Ferland 1984; Osterbrock & Ferland 2006), although other values have also been determined (Binette et al. 1990 calculate a value of 3.4). The total extinction maps are presented in Fig. 2, and shows mostly very low extinction, but some morphological features can be seen in MCG-02-12-039 and UGC 09799. Particularly high values of  $E(B - V)_{\text{internal}}$  can be seen in UGC 09799. The galactic extinction of PGC 044257 is  $E(B - V)_{\text{gal}} = 0.071$  mag, and from long-slit spectra, Crawford et al. (1999) derived the total extinction as 0.46–0.63 mag. This agrees with the extinction we derived for the very centre of the galaxy in Fig. 2, but on average our spatially resolved extinction is slightly lower. The galactic extinction  $E(B - V)_{\text{gal}}$  of UGC 09799 is 0.037 mag, and Crawford et al. (1999) derived an integrated internal extinction of  $E(B - V)_{\text{internal}}$  of 0.22 mag for the centre of this galaxy. This corresponds very well to what we derived and plotted in Fig. 2, although we find that some regions show much higher internal extinction. The values of extinction determined here may be slightly overestimated due to the choice of intrinsic H $\alpha$ /H $\beta$  flux used.

Fig. 3 shows slices with width 1 Å [smoothed spatially with Gaussian full width at half-maximum (FWHM) 1.5 spaxels and using the SAURON colour map] of PGC 026269 showing the wavelength and spatial scale over which the morphology of H $\alpha$  changes. The morphology of the nuclear region changes rapidly across the emission lines. This is illustrated in the figure showing a series of monochromatic slices. Although the continuum emission is usually smooth, the morphologies of the line emission are not uniform.

We are able to measure H $\alpha$  line fluxes with 3 A/N accuracy at around  $5 \times 10^{-18}$  erg cm $^{-2}$  s $^{-1}$ . After correcting for extinction, we are able to measure the following lines within our wavelength range: [Ar IV]  $\lambda 4740$  Å; H $\beta$   $\lambda 4861$  Å; [O III]  $\lambda\lambda 4958, 5007$  Å; [N I]  $\lambda\lambda 5198, 5200$  Å; He I  $\lambda 5876$  Å; [O I]  $\lambda\lambda 6300, 6364$  Å; [N II]  $\lambda\lambda 6548, 6583$  Å; H $\alpha$  at 6563 Å; [S II]  $\lambda\lambda 6716, 6731$  Å (see Figs 4–19 for the A/N ratios of the individual emission lines). H $\alpha$  and [N II]  $\lambda\lambda 6548, 6583$  Å have already been measured for MCG-02-12-039 and UGC 09799, and H $\beta$  and [O III]  $\lambda\lambda 4958, 5007$  Å have also been measured for UGC 09799. All the other line measurements are new.

## 5 INDIVIDUAL GALAXIES

The continuum emission of the galaxies is shown in Fig. 1. Figs 20, 6, 10 and 14 show a random spectrum in the central region of MCG-02-12-039, PGC 026269, PGC 044257 and UGC 09799, respectively. The best-fitting stellar template, Gaussians at the emission lines, best-fitting stellar templates with the emission lines subtracted and the relative flux for the measured emission lines are also shown. The absorption-extracted, dereddened maps of the H $\alpha$ , [N II]  $\lambda 6583$ /H $\alpha$ , and [O III]  $\lambda 5007$ /H $\beta$  emission are shown in Fig. B1.

For comparison purposes, the kinematics were extracted from the IFU image along the same slit position as the long-slit data in Loubser et al. (2008, hereafter Paper I). This comparison for MCG-

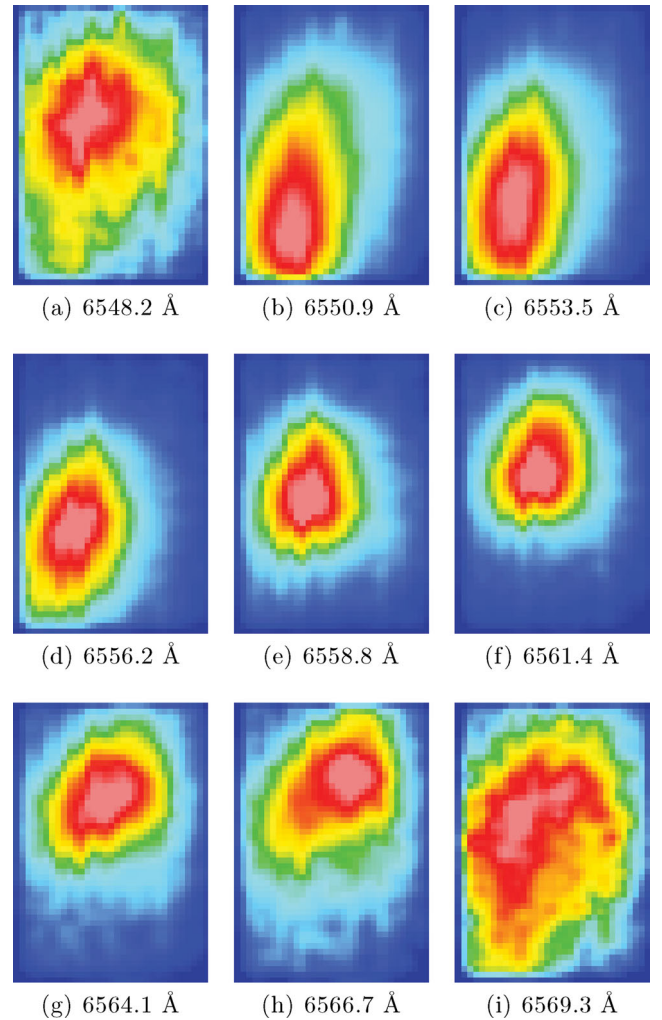


**Figure 3.** Slices of width 1 Å (smoothed spatially with Gaussian FWHM 1.5 spaxels and using a SAURON colour map) of PGC 026269 showing the wavelength and spatial scale over which the transition from [N II]  $\lambda 6548$  to H $\alpha$  emission occurs, and how the morphology of H $\alpha$  changes. Although the continuum emission is usually smooth, the morphologies of the line emission are not uniform.

02-12-039, PGC 026269 and PGC 044257 is showed in Appendix A, and the data points compare satisfactory.

The absorption-extracted, dereddened maps of the H $\alpha$  emission are shown in Fig. B1 in units of  $10^{-15}$  erg cm $^{-2}$  s $^{-1}$ . We also show the useful ratios [N II]  $\lambda 6583$ /H $\alpha$  and [O III]  $\lambda 5007$ /H $\beta$ . Figs 4–18 show the A/N of the H $\alpha$ , [N II]  $\lambda 6583$  Å; [S II]  $\lambda\lambda 6716, 6731$  Å; [O III]  $\lambda 5007$  Å; [O I]  $\lambda 6300$  Å lines. As mentioned in the Introduction, MCG-02-12-039 and UGC 09799 already have previous IFU observations which is compared (in terms of S/N and lines measurable) in the beginning of Section 3 and the last paragraph of Section 4. The stellar kinematics in Figs 21, 7, 11 and 16 were measured using all the absorption lines within our wavelength range.

For a sample of  $\sim 50$  elliptical galaxies, Sarzi et al. (2006) find ionized gas velocities (estimated using the [O III]  $\lambda 5007$  line) between  $-250$  and  $250$  km s $^{-1}$ , and gas velocity dispersion as high as  $250$  km s $^{-1}$ . Using the same line, we find gas velocities from  $\pm 100$  to  $\pm 350$  km s $^{-1}$ , and line widths from 200 to 420 km s $^{-1}$ . Using H $\alpha$ , we find gas velocities from  $\pm 125$  to  $\pm 350$  km s $^{-1}$ , and line widths from 200 to 400 km s $^{-1}$ .

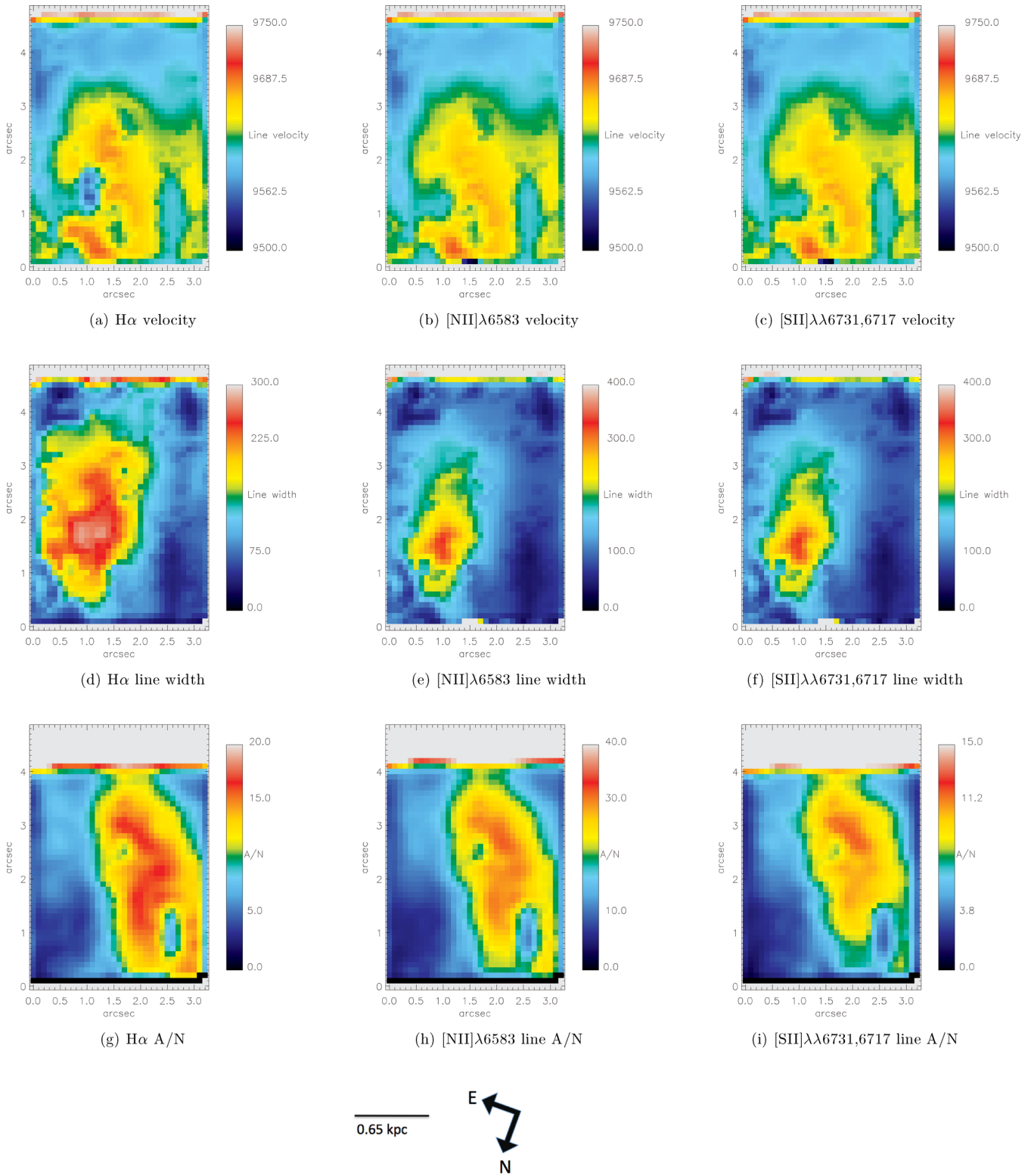


**Figure 4.** MCG-02-12-039: velocity (in km s $^{-1}$ ), line width (in km s $^{-1}$ ) and A/N of the H $\alpha$ , [N II]  $\lambda$ 6583 and [S II]  $\lambda\lambda$ 6731, 6717 lines.

### 5.1 MCG-02-12-039

The central galaxy (MCG-02-12-039) of Abell 0496 is a fairly weak line emitter (Fabian et al. 1981; Hu, Cowie & Wang 1985) and is host to the compact radio source MSH 04–112 (Marković, Owen & Eilek 2004). Abell 0496 is a relaxed cluster with a cool

core with a central metal abundance enhancement (Tamura et al. 2001). At a redshift of 0.0329, the galaxy has a linear scale of 0.656 kpc arcsec $^{-1}$  (from Hatch et al. 2007). This cluster has an interesting H $\alpha$  morphology (McDonald et al. 2010). There are at least five distinct filaments, with various shapes and directions. The two longest filaments run parallel to each other for  $\sim$ 12 kpc

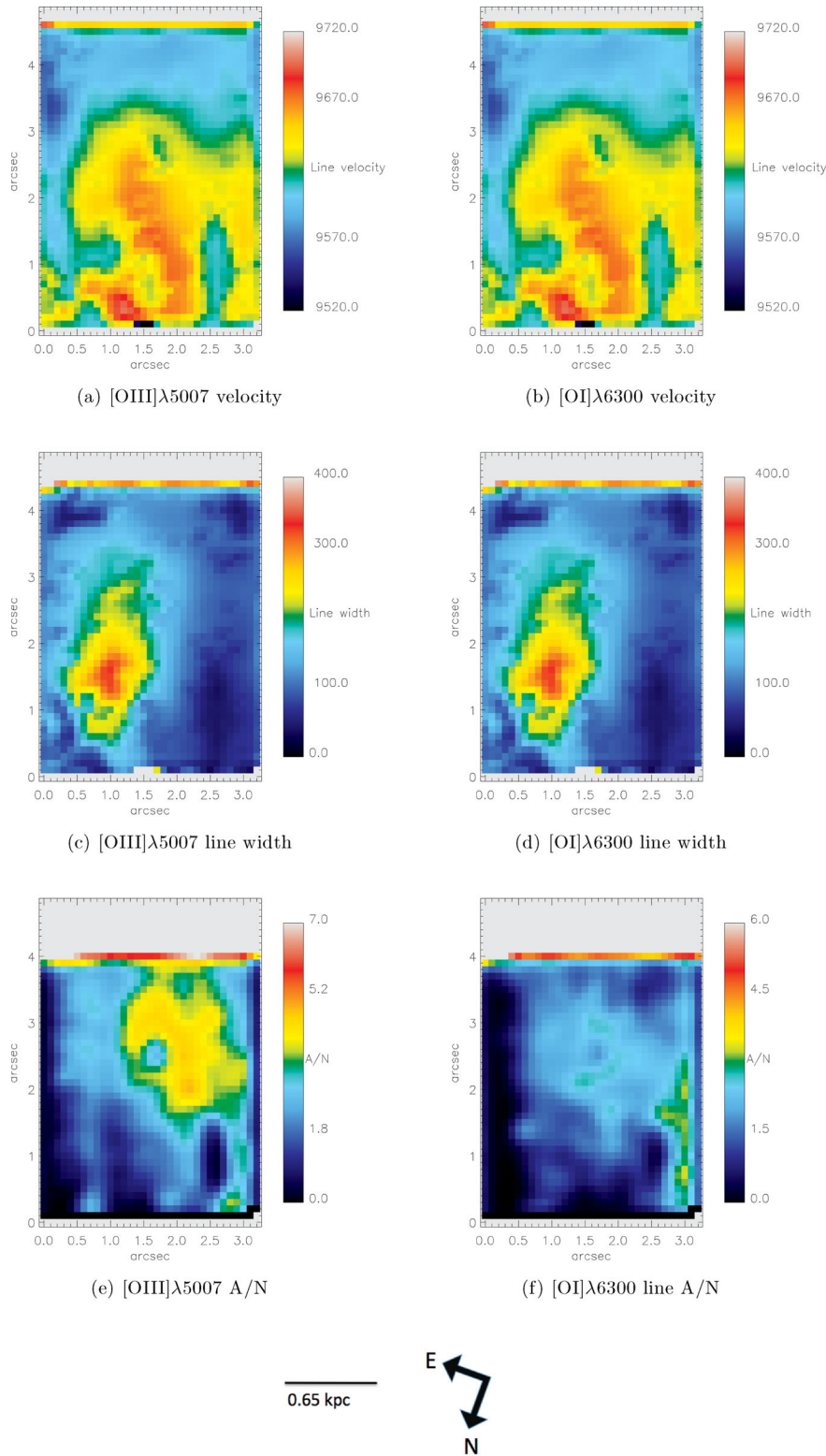


**Figure 5.** MCG-02-12-039: velocity (in  $\text{km s}^{-1}$ ), line width (in  $\text{km s}^{-1}$ ) and A/N of the  $[\text{O III}] \lambda 5007$  and  $[\text{O I}] \lambda 6300$  lines.

(18.3 arcsec, whereas our observations only cover 3.5 by 5 arcsec in the centre).

Fig. B1 shows that the peak  $\text{H}\alpha$  emission is also where the dust (extinction) is the highest in Fig. 2. This is similar to the finding of Hatch et al. (2007), where they found that the peak  $\text{H}\alpha + [\text{N II}]$  emission corresponds to the area where the three dust lanes meet

in the galaxy centre. We confirm the observation by Hatch et al. (2007) that the line emission follows the general path of the dust (extinction) features, but is not as filamentary.

IFU observations of this galaxy was also taken by Hatch et al. (2007), but they only measured the  $\text{H}\alpha$  and  $[\text{N II}] \lambda\lambda 6548, 6583 \text{\AA}$  lines. Their spectral resolution is much poorer at  $223\text{--}273 \text{ km s}^{-1}$

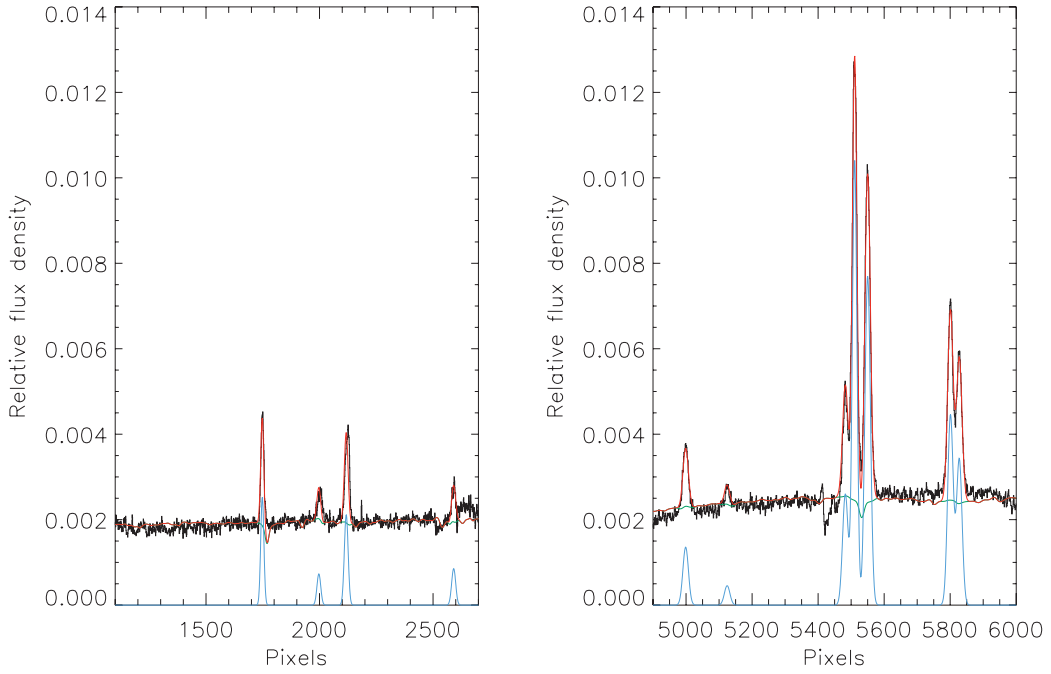


**Figure 6.** A random spectrum in the central region of PGC 026269. The red line indicates the best-fitting stellar template and Gaussians at the emission lines, and the green line indicates the best-fitting stellar templates with the emission lines subtracted. The blue line indicates the relative flux for the measured emission lines. The lines are (from left to right) in the left-hand plot: H $\beta$ , the [O III] doublet and [N I], and in the right-hand plot: [O I] doublet, [N II], H $\alpha$ , [N II] and the [S II] doublet. The sharp feature to the left of the first [N II] line is one of the two CCD chip gaps and was masked during the ppxf and GANDALF fitting processes.

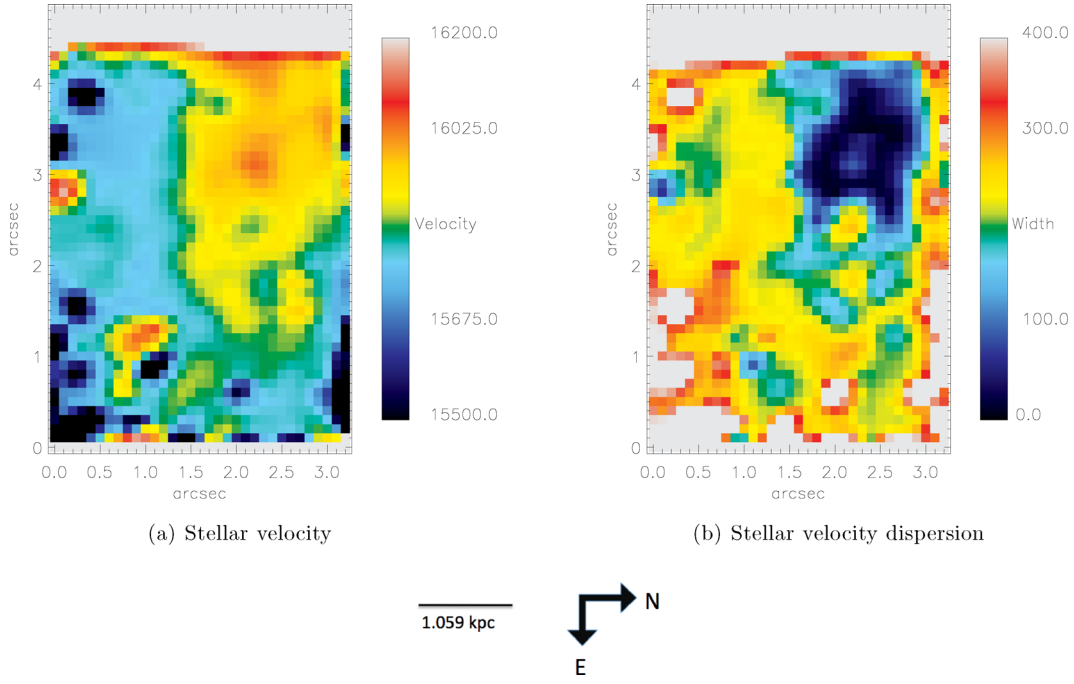


**Figure 7.** PGC 026269: velocity and velocity dispersion of the absorption lines in  $\text{km s}^{-1}$ .

than ours at  $81 \text{ km s}^{-1}$ . Our S/N is also more than five times that of Hatch et al. (2007), observed with a much bigger instrument. We plot H $\alpha$ , [N II], [S II], [O III] and [O I] velocities, line width and A/N in Figs 4 and 5. The stellar component displays an elongated morphology in the kinematics plotted in Fig. 21. The gas components also appear elongated (kinematics plotted in Fig. 4), but to a lesser extent. It suggests that the stars and gas are kinematically de-

coupled. Comparison of the gas kinematics (Figs 4 and 5) with the stellar kinematics presented in Figs 21 and A1, as well as by Fisher, Illingworth & Franx (1995) confirms the Hatch et al. (2007) observations that the two components are disconnected. Comparison of the plots in Fig. 4 showed that, to the degree that our spatial resolution reveals, it appears that all the optical forbidden and hydrogen recombination lines originate in the same gas.

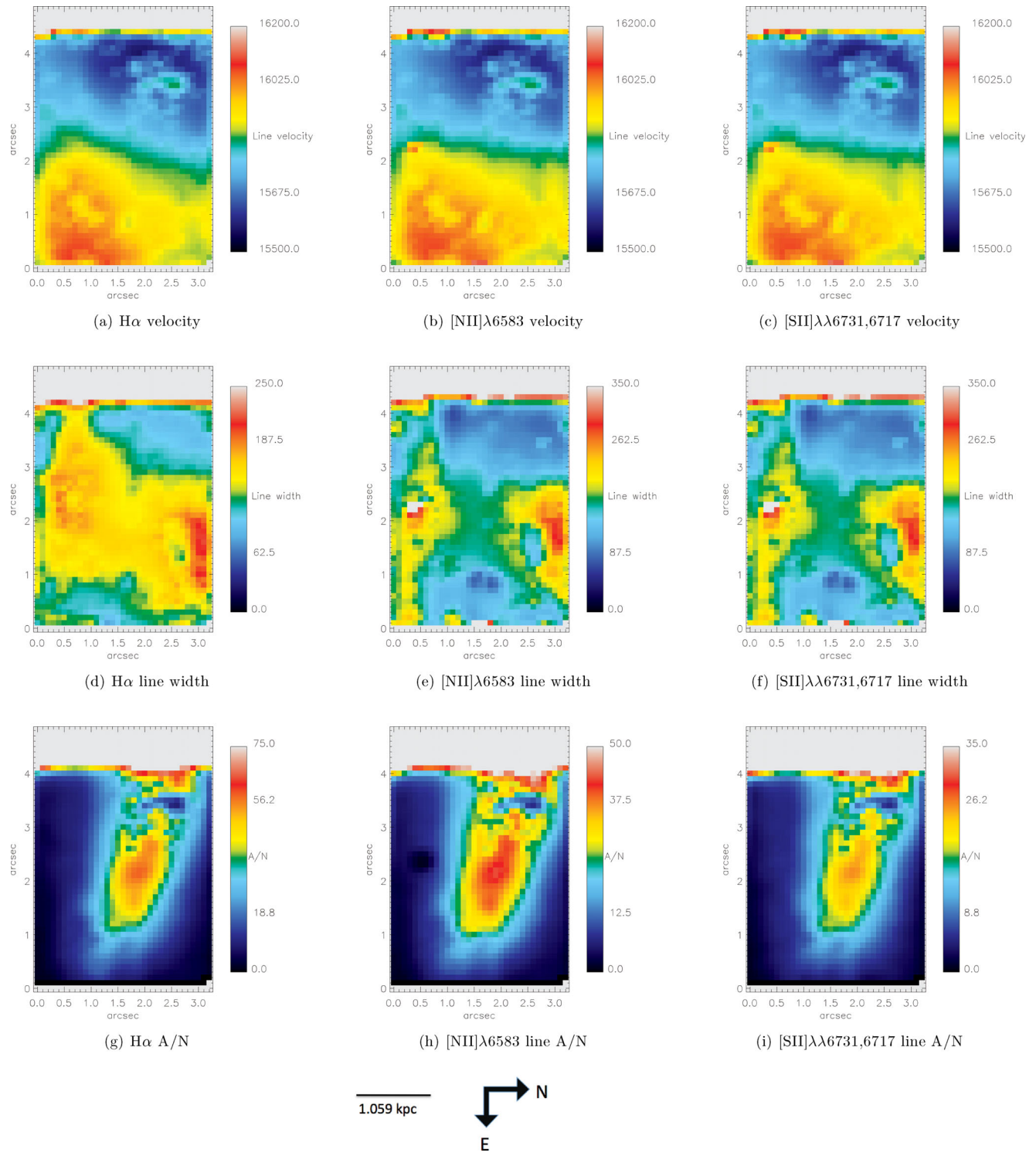


**Figure 8.** PGC 026269: velocity (in  $\text{km s}^{-1}$ ), line width (in  $\text{km s}^{-1}$ ) and A/N of the  $\text{H}\alpha$ ,  $[\text{N II}]\lambda 6583$  and  $[\text{S II}]\lambda\lambda 6731, 6717$  lines.

We find a maximum emission line width of  $400 \text{ km s}^{-1}$  as shown in Figs 4 and 5. This is again similar to the finding of Hatch et al. (2007). They found a maximum line width of  $600 \text{ km s}^{-1}$  in the dust-free central region to the north-east of the galaxy centre, and the rest of the nebula to have a line width of  $100\text{--}250 \text{ km s}^{-1}$ .

The stellar line-of-sight velocity reveals that some parts of the nucleus are blueshifted by  $\sim 125 \text{ km s}^{-1}$  and some parts are red-

shifted by the same amount. Hatch et al. (2007) found the southern part of the galaxy to be blueshifted by  $-200 \text{ km s}^{-1}$  whilst the northern section is marginally redshifted up to  $+150 \text{ km s}^{-1}$ . No clear kinematic pattern is associated with the dust structures.

The peak-to-peak gas velocity of  $250 \text{ km s}^{-1}$  is fairly low compared to the other CCGs, and the stellar component of Abell 0496 has a mean rotation of  $59 \text{ km s}^{-1}$  (Paper I).

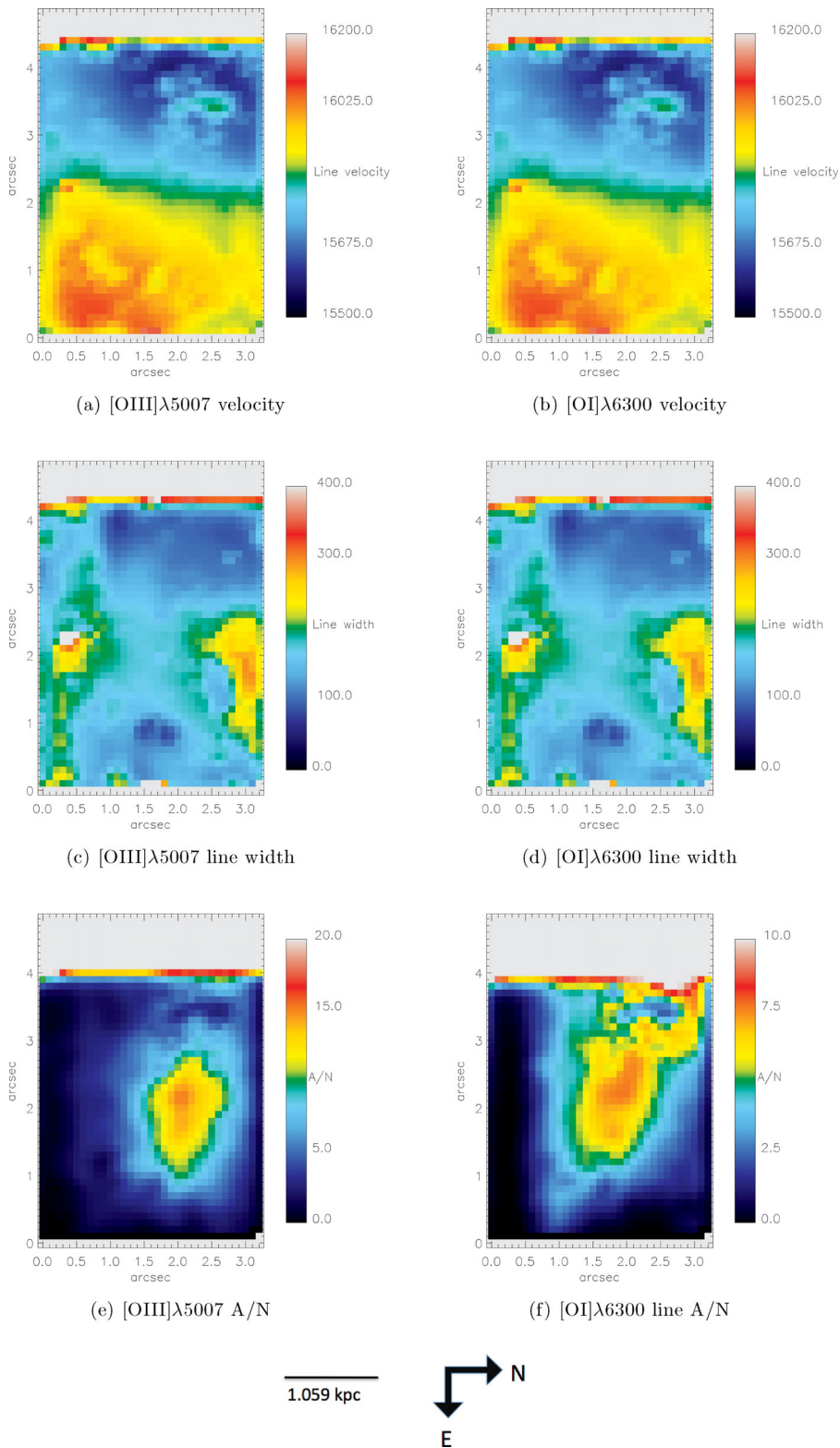


**Figure 9.** PGC 026269: velocity (in  $\text{km s}^{-1}$ ), line width (in  $\text{km s}^{-1}$ ) and A/N of the  $[\text{O III}] \lambda 5007$  and  $[\text{O I}] \lambda 6300$  lines.

## 5.2 PGC 026269

This galaxy coincides with the well-known luminous radio counterpart Hydra A. Abell 0780 is a poor cluster with an associated cooling flow nebulae. IFU observations of this

galaxy have not been presented in the literature before this study.

The stellar line-of-sight velocity (from the IFU data) is blue- and redshifted by  $\sim 175 \text{ km s}^{-1}$  which is slightly higher than that derived from long-slit spectroscopy ( $51 \pm 20 \text{ km s}^{-1}$ ; Paper I).

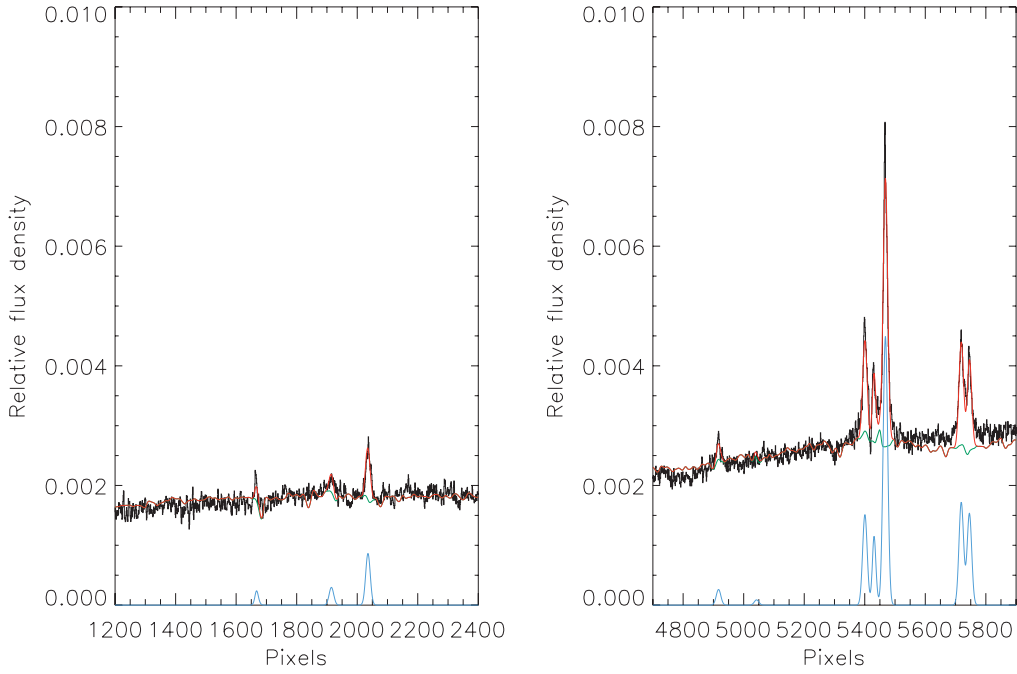


**Figure 10.** A random spectrum in the central region of PGC 044257. The red line indicates the best-fitting stellar template and Gaussians at the emission lines, and the green line indicates the best-fitting stellar templates with the emission lines subtracted. The blue line indicates the relative flux for the measured emission lines. The lines are (from left to right) in the left-hand plot: H $\beta$  and the [O III] doublet, and in the right-hand plot: [O I] doublet, [N II], H $\alpha$ , [N II] and the [S II] doublet.

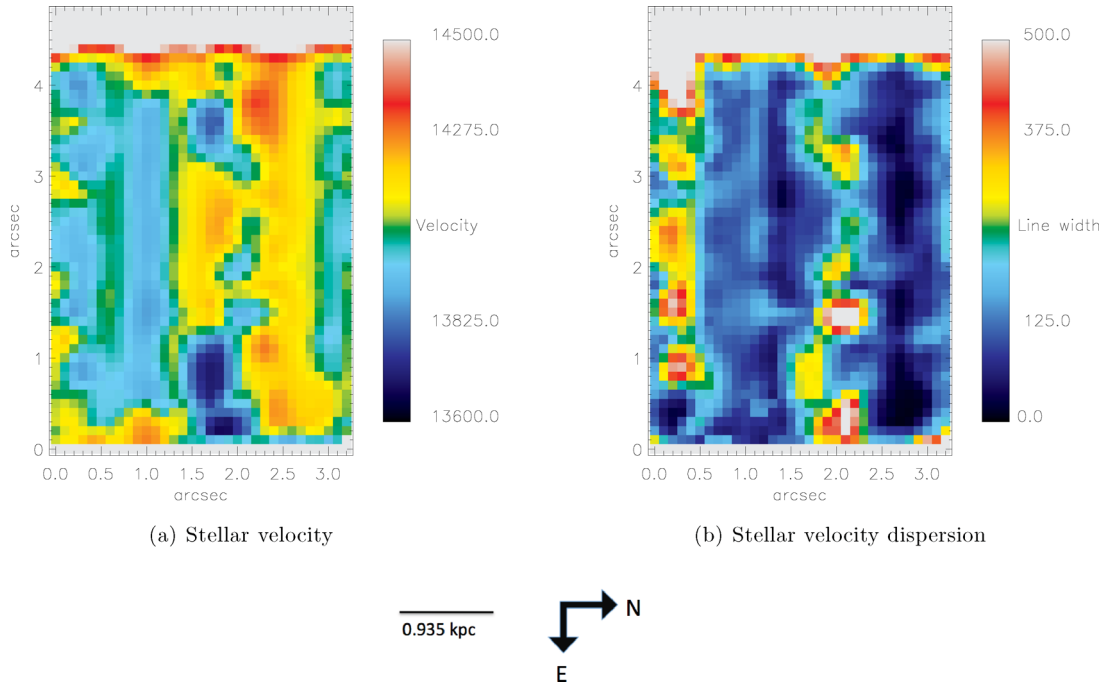


**Figure 11.** PGC 044257: velocity and velocity dispersion of the absorption lines in  $\text{km s}^{-1}$ .

We plot the kinematics of the stellar and gaseous components in Figs 7 and 8. Both the stellar and gaseous components show clear rotation in Figs 7 and 8, although it also seems to be decoupled. This system bears resemblance to the BCG NCG 3311 in Abell 1060, studied by Edwards et al. (2009) which also showed striking rotation. The rotation of the warm gas agrees with the long-slit observations by McDonald et al. (2012).

We plot H $\alpha$ , [N II], [S II], [O III] and [O I] velocities, line width and A/N in Figs 8 and 9. Comparison of the plots in Fig. 4 showed that, to the degree that our spatial resolution reveals, it appears that all the optical forbidden and hydrogen recombination lines originate in the same gas.

Wise et al. (2007) present a summary of the X-ray and radio properties of this cluster, showing the excellent correlation between

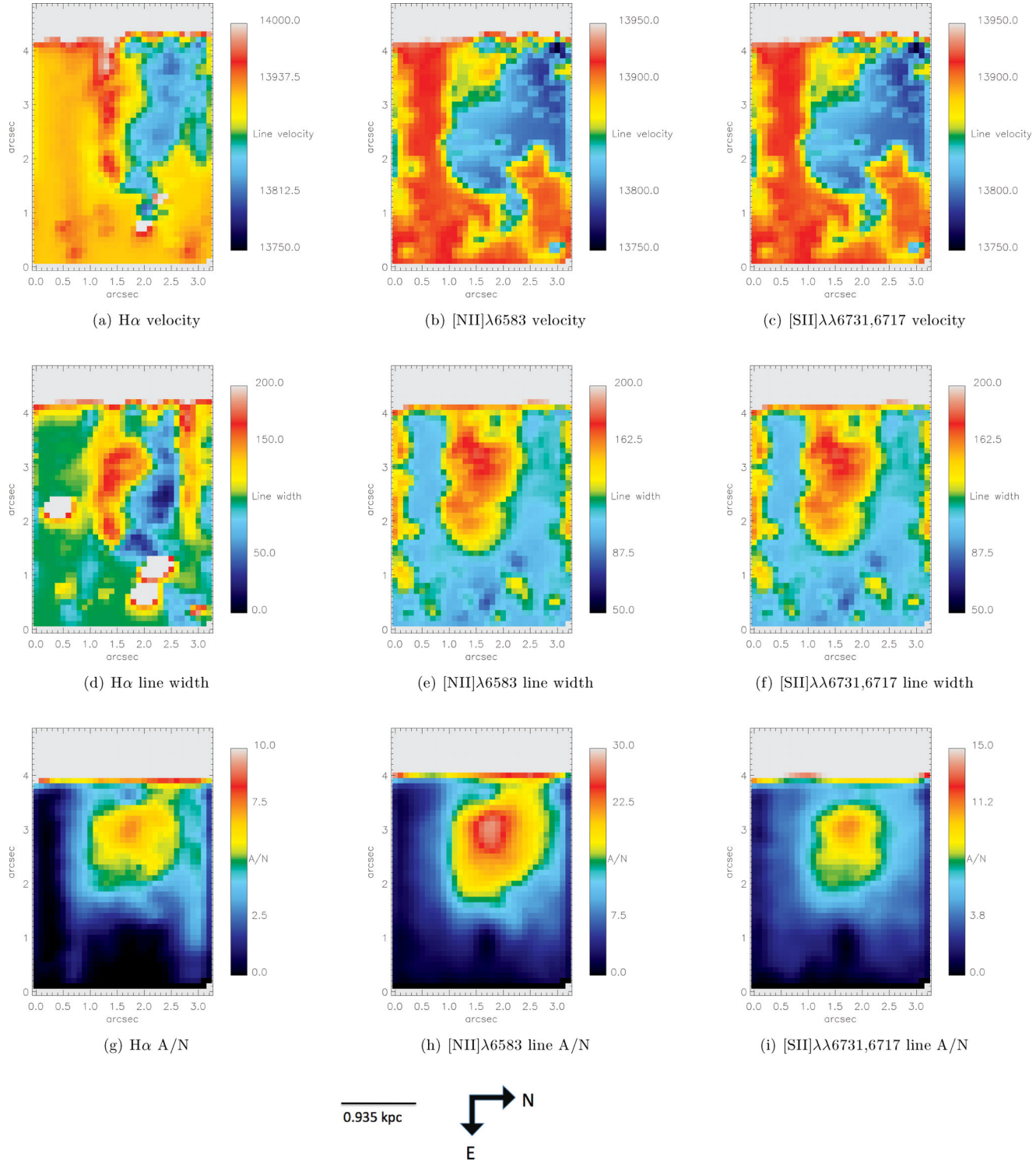


**Figure 12.** PGC 044257: velocity (in  $\text{km s}^{-1}$ ), line width (in  $\text{km s}^{-1}$ ) and A/N of the  $\text{H}\alpha$ ,  $[\text{N II}] \lambda 6583$  and  $[\text{S II}] \lambda\lambda 6731, 6717$  lines.

the radio jets and the X-ray cavities. The arcing  $\text{H}\alpha$  filament that McDonald et al. (2010) detect north of the CCG (on a larger scale as this study) appears to be spatially correlated with the radio jet. Figs 22(d)–(f) show that our optical observations confirm that the photoionization is caused by an AGN (the green and red curves), and are therefore consistent with the X-ray and radio studies of this system on larger scales.

### 5.3 PGC 044257

This CCG is one of the rare cases (occurs in  $\sim 3$  per cent of CCGs; Hamer et al. 2012) where the CCG is slightly offset from the optical line emission (Johnson et al. 2010). The rarity of such offsets points to a large event in cluster evolution, a major cluster merger or possibly a powerful AGN outburst. Whatever the reason for the

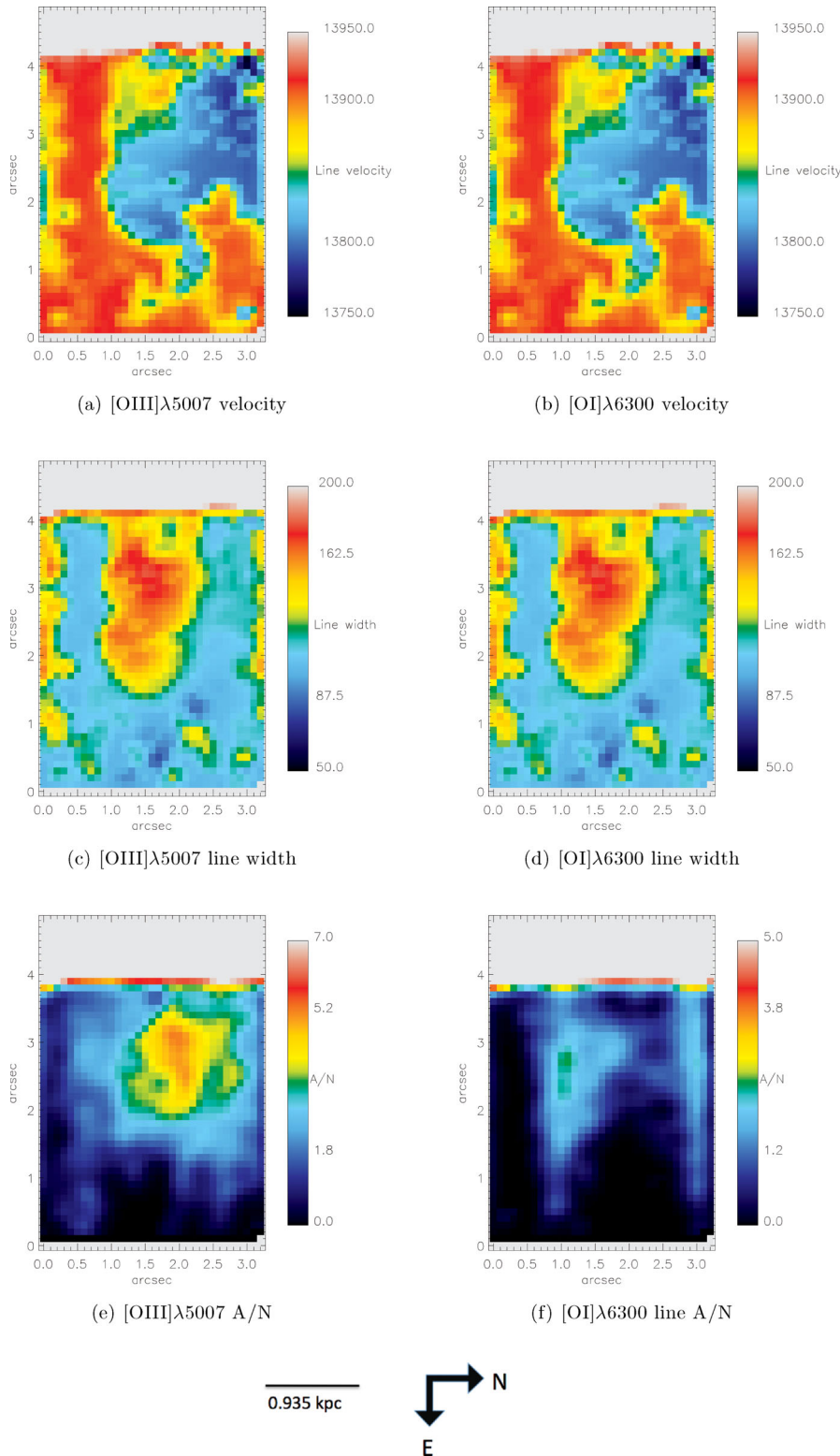


**Figure 13.** PGC 044257: velocity (in  $\text{km s}^{-1}$ ), line width (in  $\text{km s}^{-1}$ ) and A/N of the  $[\text{O III}] \lambda 5007$  and  $[\text{O I}] \lambda 6300$  lines.

separation the gas cooling at the X-ray peak will continue and cooled gas will be deposited away from the CCG (Hamer et al. 2012).

IFU observations of this galaxy have not been presented in the literature before this study. The stellar line-of-sight velocity is blue-

and redshifted by  $\sim 225 \text{ km s}^{-1}$  which is higher than derived from long-slit spectroscopy ( $20 \pm 16 \text{ km s}^{-1}$ ; Paper I).

We plot the kinematics of the stellar and gaseous components in Figs 11 and 12. Both the stellar and gaseous components show morphologies (Figs 11 and 12) that are elongated and aligned. However

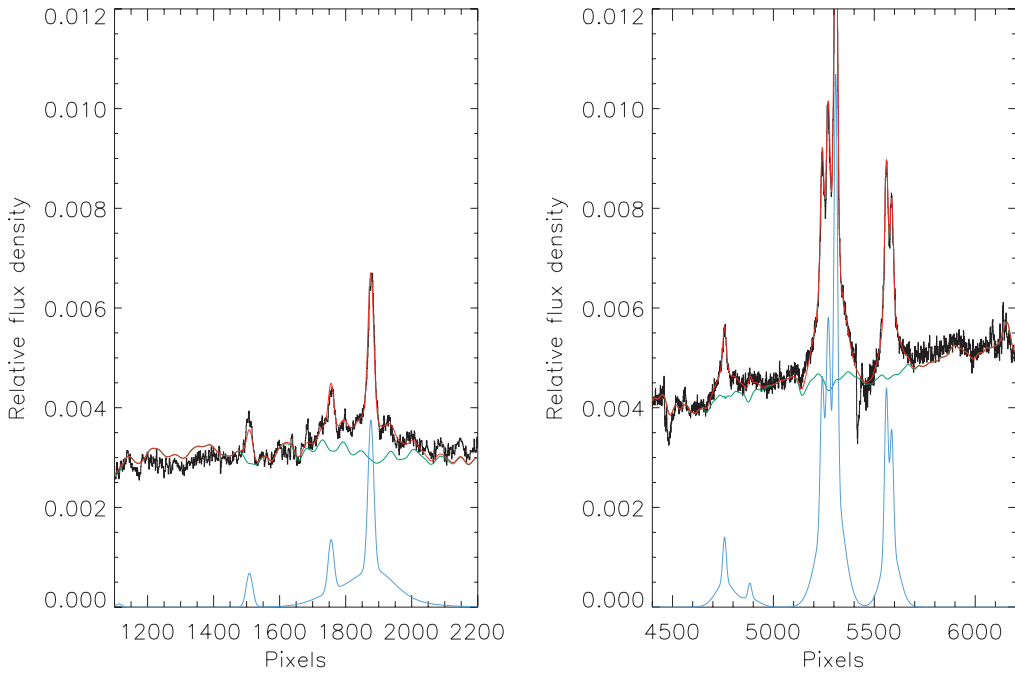


**Figure 14.** A random spectrum in the central region of UGC 09799. The red line indicates the best-fitting stellar template and Gaussians at the emission lines, and the green line indicates the best-fitting stellar templates with the emission lines subtracted. The blue line indicates the relative flux for the measured emission lines. The lines are (from left to right) in the left-hand plot: H $\beta$  and the [O III] doublet, and in the right-hand plot: [O I] doublet, [N II], H $\alpha$ , [N II] and the [S II] doublet. The sharp feature between the [N II] and [S II] lines is one of the two CCD chip gaps and was masked during the ppxf and GANDALF fitting processes.

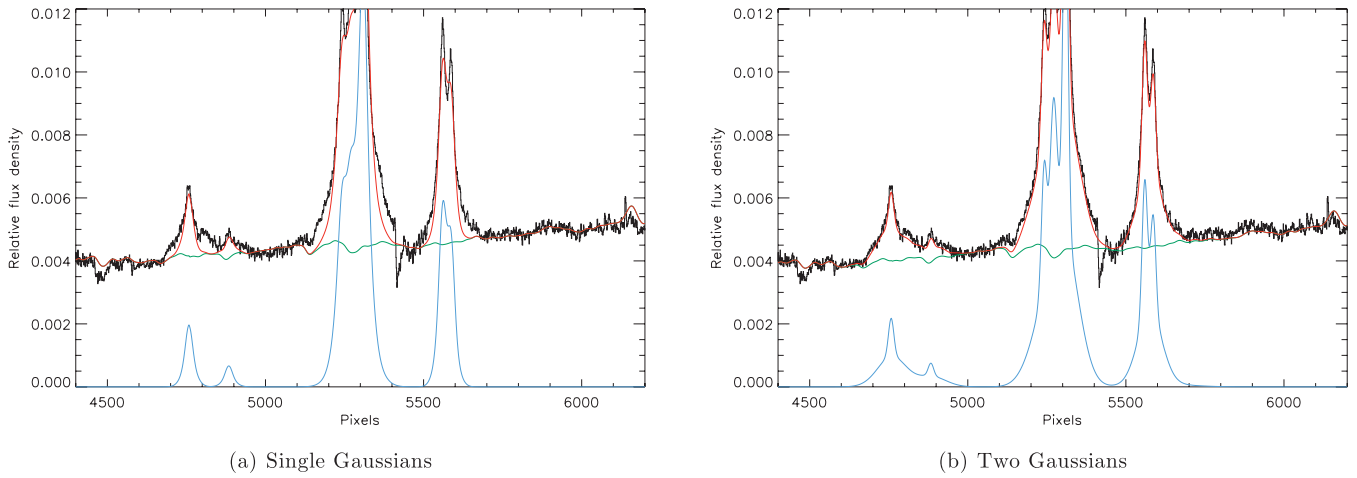


**Figure 15.** UGC 09799 showing single Gaussian fits and double Gaussian fits (one narrow and one broad) to the [O I] doublet, [N II], H $\alpha$ , [N II] and the [S II] doublet.

the recession velocity of the gas is  $\sim 200$  km s $^{-1}$ , which is higher than that of the stars, suggesting that the gaseous and stellar components are decoupled. The rotation of the warm gas agrees with the long-slit observations by McDonald et al. (2012).

We plot H $\alpha$ , [N II], [S II], [O III] and [O I] velocities, line width and A/N in Figs 12 and 13. To the degree that our spatial resolution reveals, it appears that all the optical forbidden and hydrogen recombination lines originate in the same gas.

We find the H $\alpha$  flux to be uniform in Fig. B1 suggesting that all of the gas had the same origin, but the H $\alpha$  flux is also quite low. If Fig. B1 is compared to Fig. 12, then it can be seen that some structure is visible where the A/N of H $\alpha$  is the highest. The H $\alpha$  appear to be quite core dominated. McDonald et al. (2010) found

that the direction of the H $\alpha$  filaments (from narrow band imaging) correlate with the position of nearby galaxies. The filaments in Abell 1644 also appear to be star forming (McDonald et al. 2011). The star-forming filaments that McDonald et al. (2011) detected are on a bigger scale than the region we probe in this study. Our results show that the very centre of the system displays properties of a LINER (see Section 6), and therefore both mechanisms may be part of this system at different scales.

#### 5.4 UGC 09799

IFU observations of this galaxy (around H $\alpha$  and H $\beta$ ) were previously presented by Edwards et al. (2009). The observations

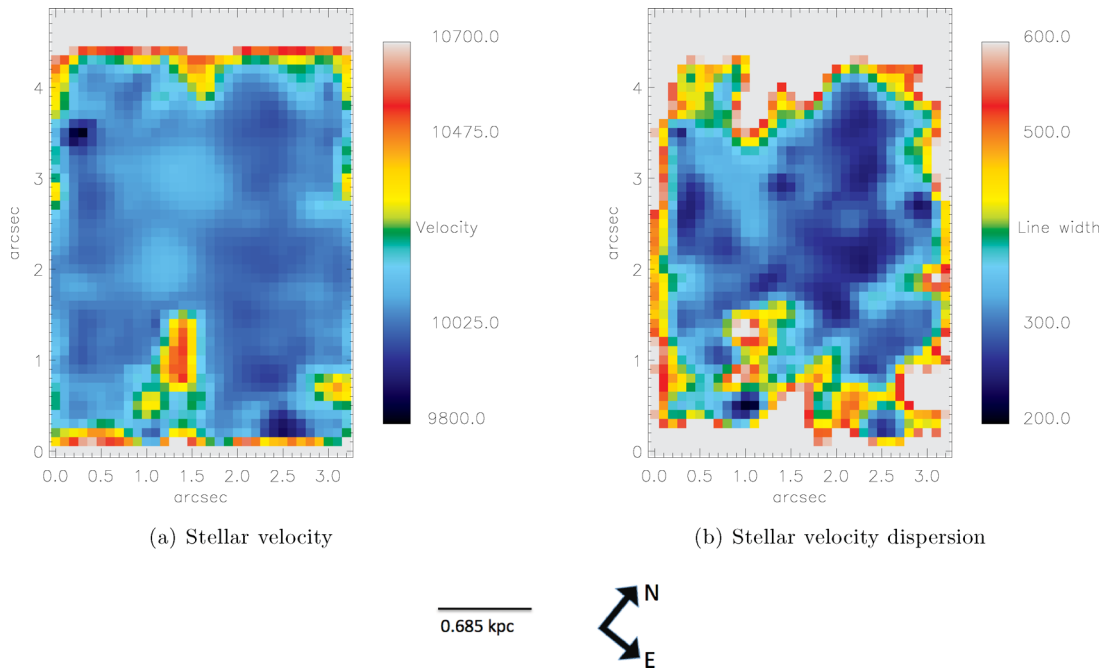


**Figure 16.** UGC 09799: velocity and velocity dispersion of the absorption lines in  $\text{km s}^{-1}$ .

presented in this study are improved in that it was observed with triple the integration time of the previous observations. The morphology of the continuum emission of this galaxy (see Fig. 1) is centrally concentrated and condensed, as was also found by Edwards et al. (2009).

Just fitting one single Gaussian per emission line resulted in very poor fits (as shown in Fig. 15). We also tried fitting Voigt profiles to the [O III] lines, for example, as well as slightly offset blue and red velocity wings. The best fits were consistently achieved using 2 Gaussians for each individual line in the [O III], [O I], [N II] and [S II] doublets, of which one of the Gaussians was broader than the other. The H $\beta$  lines (and therefore also H $\alpha$ ) however required no additional Gaussian to achieve a good fit. Edwards et al. (2009) could not detect H $\beta$  emission above the  $1\sigma$  level for this galaxy. We do detect H $\beta$  above this level and plot the flux ratios in Fig. B1. Fig. 14 in Edwards et al. (2009) can be compared with Figs 17 and B1 here – both show smooth centrally condensed emission.

We plot the kinematics of the stellar and gaseous components in Figs 16 and 17. We plot H $\alpha$ , [N II], [S II], [O III] and [O I] velocities, line width and A/N in Figs 17 and 18. To the degree that our spatial resolution reveals, it appears that all the optical forbidden and hydrogen recombination lines originate in the same gas. Our kinematic analysis can be compared to that of Edwards et al. (2009), who detected a gradient in the velocity but could not differentiate between a rotation and outflow. Our stellar kinematics are shown in Fig. 16, however, we do not detect rotational kinematics. Edwards et al. (2009) also found H $\alpha$  to have a velocity range of  $-250$  to  $+150 \text{ km s}^{-1}$ . Our H $\alpha$  kinematics are shown in Fig. 17 and show also a range ( $\sim 400 \text{ km s}^{-1}$ ) of velocities for H $\alpha$ . The gaseous components show rotation in Fig. 17 even though no rotation is apparent in the stellar components (Fig. 16).

This galaxy has patchy dust in the centre (Laine et al. 2003, also shown in Fig. 2), and Hicks & Mushotzky (2005) have deduced star formation from the excess UV–IR emission. The far-UV/H $\alpha$  ratio suggests heating by fast shocks or some other source of hard ionization (e.g. cosmic rays, AGN). The filaments of Abell 2052

have ratios which are consistent with this picture (McDonald et al. 2011). The highest extinction (in Fig. 2) does not coincide with the H $\alpha$  peak (Appendix B1), and is slightly off centre. This does not necessarily contrast with the results quoted by Laine et al. (2003) that the dust is patchy in the centre, as the centre of the observations might not necessarily be exactly the same as our IFU placement (see Fig. 1). Fig. 1 also shows that our continuum emission is smooth, similar to the conclusion reached by Edwards et al. (2009).

Venturi, Dallacasa & Stefanachi (2004) found a parsec-scale bipolar radio source, and *Chandra* X-ray emission shows two bubbles in the ICM on a larger scale (Blanton, Sarazin & McNamara 2003). Our results are consistent with the central emission being that of a LINER (see Section 6).

## 6 DISCUSSION – IONIZATION MECHANISMS

Various mechanisms have been proposed as sources of excitation in the nebulae, including photoionization by radiation from the AGN, cluster X-rays or hot stars, collisional heating by high-energy particles, shocks or cloud–cloud collisions and conduction of heat from the X-ray corona (Peterson et al. 2003). However, none so far satisfactorily describes all the characteristic spectra, energetics and kinematics of the extended emission-line regions (Wilman et al. 2006; Hatch et al. 2007).

We reiterate that the FOV of the observations is only  $3.5 \times 5 \text{ arcsec}^2$  (corresponding to the central few parsec – see Table 1). These results only look at the very heart of these sources. Therefore, it is really only the emission mechanisms for the gas at the very centre of these systems that is being studied here.

The forbidden lines such as [N II]  $\lambda 6583$  result from the excitation of N $^+$  through collisions with electrons liberated through photoionization. The H $\alpha$  emission results from the recombination of the hydrogen ion. [N II]  $\lambda 6583$  flux depends on the N $^+$  abundance, the strength of the radiation field and the form of the radiation field: a harder ionizing source will produce a greater flux. The H $\alpha$  flux also depends on the strength of the radiation field. Therefore, the

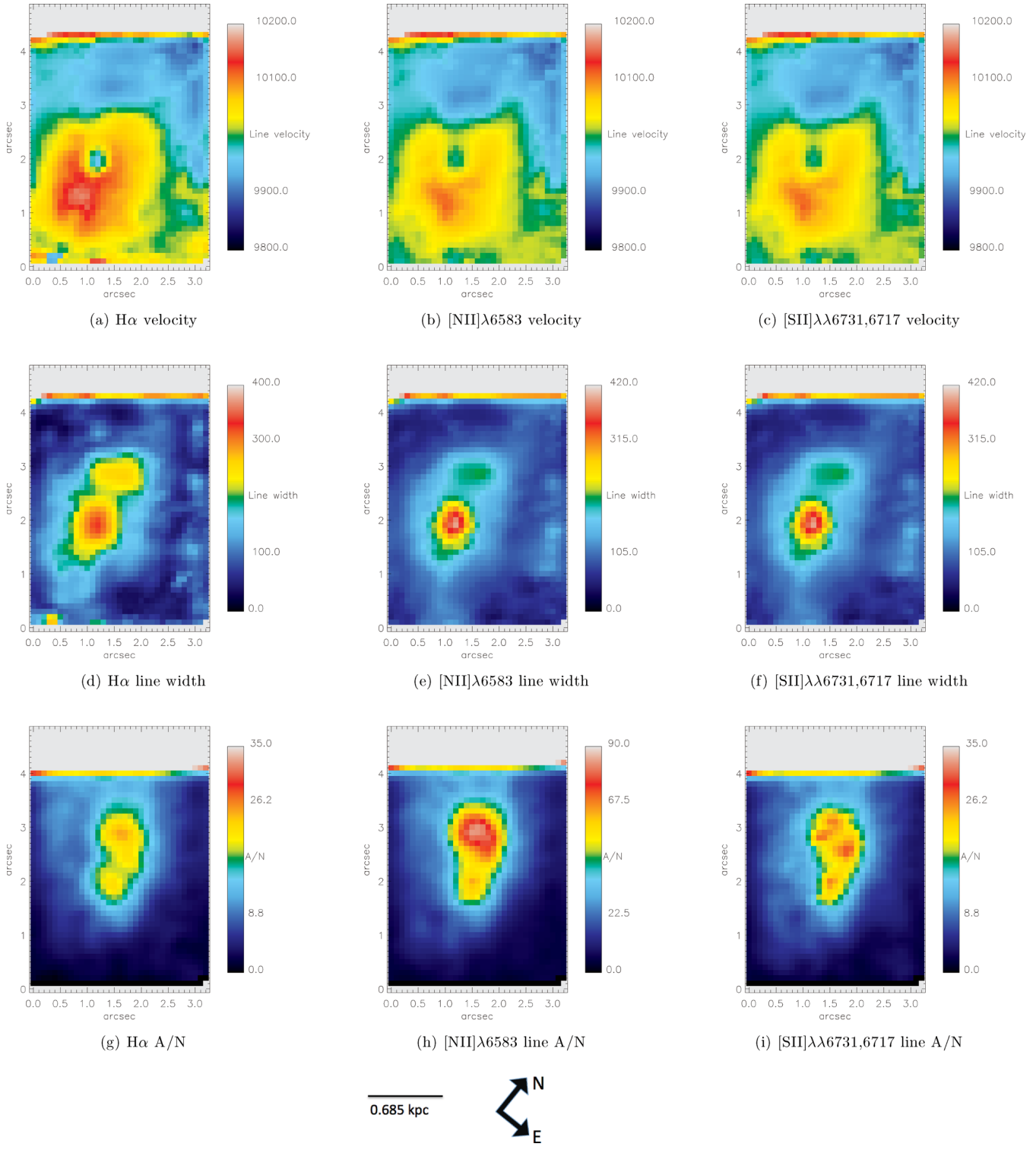


**Figure 17.** UGC 09799: velocity (in km s $^{-1}$ ), line width (in km s $^{-1}$ ) and A/N of the H $\alpha$ , [N II]  $\lambda$ 6583 and [S II]  $\lambda\lambda$ 6731, 6717 lines.

ratio will depend on the metallicity of the gas and the form of the ionizing radiation. The form of the ionizing radiation and/or the gas metallicity is not uniform but must vary within each galaxy and between the whole sample. Different excitation mechanisms may act in different regions (Hatch et al. 2007; Edwards et al. 2009), or the H $\alpha$  emission might be disturbed by the presence of companion galaxies (Wilman et al. 2006).

A commonly used method to distinguish between the sources of ionization uses the emission-line diagrams pioneered by Baldwin, Phillips & Terlevich (1981, hereafter BPT diagram) which separate the two major origins of emission: star formation and AGN. The diagrams use pairs of emission line ratios, of which the most commonly used is [O III]  $\lambda$ 5007/H $\beta$  against [N II]  $\lambda$ 6584/H $\alpha$ . Extinction-corrected emission-line measurements were used (even though the

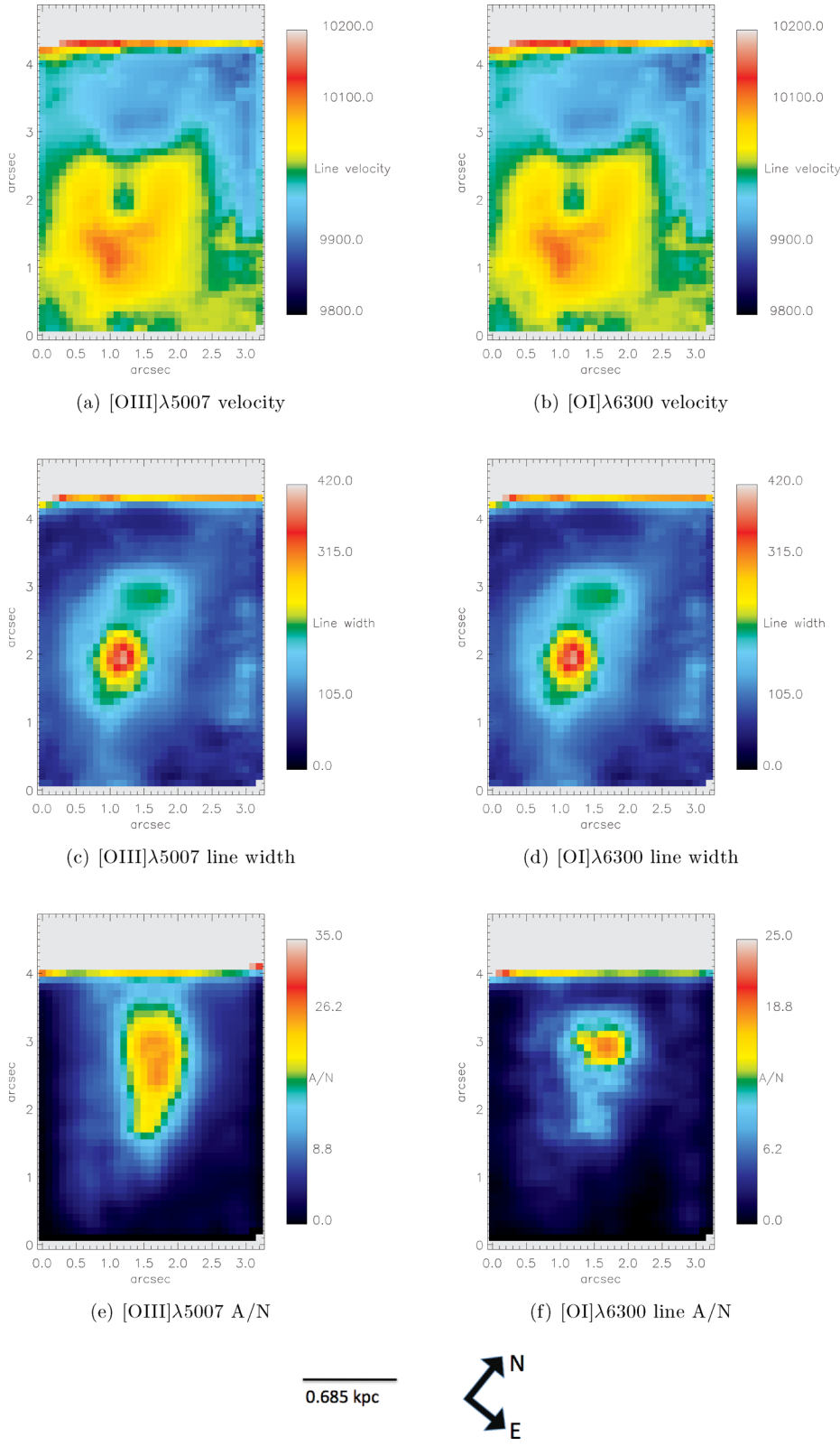


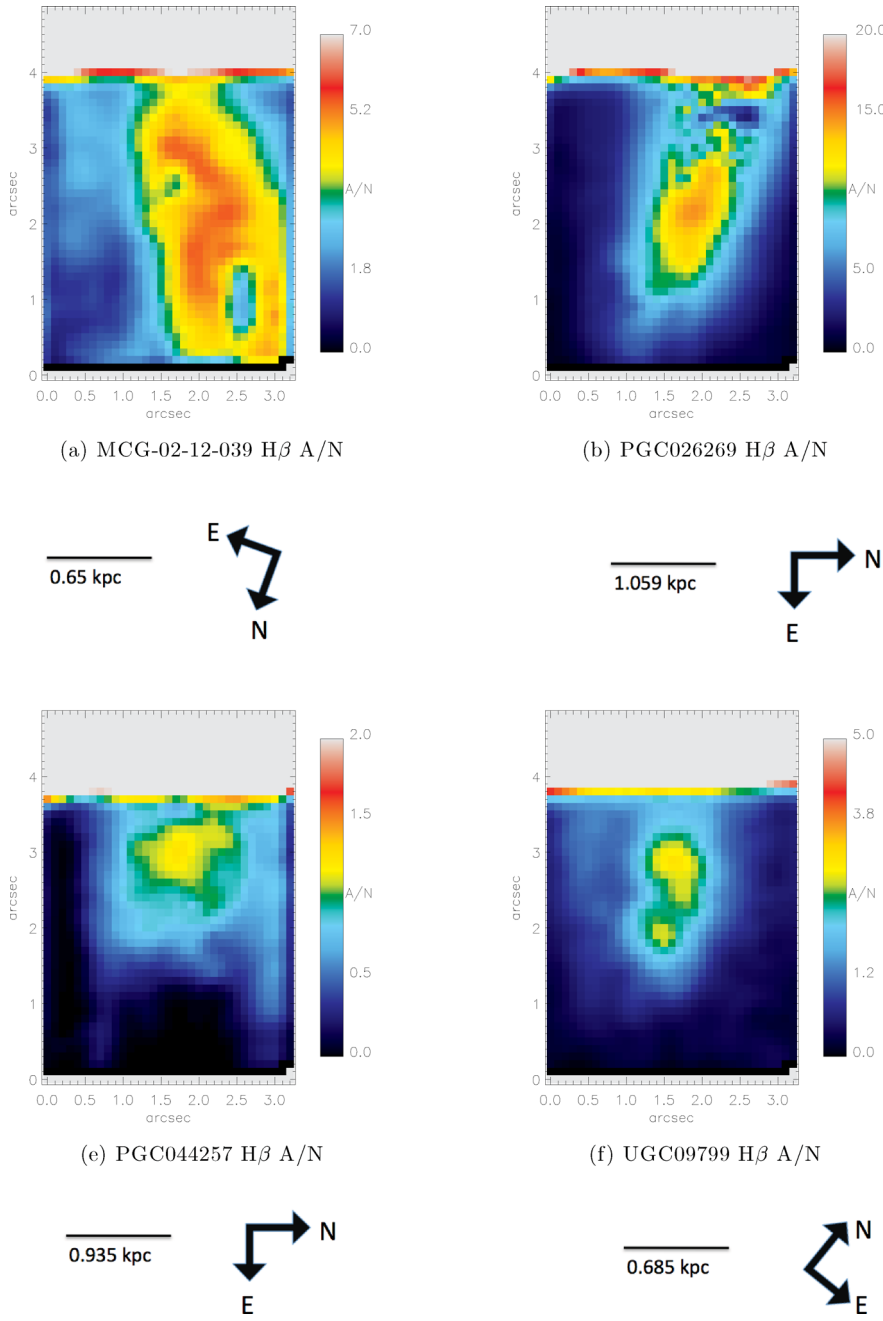
**Figure 18.** UGC 09799: velocity (in  $\text{km s}^{-1}$ ), line width (in  $\text{km s}^{-1}$ ) and A/N of the  $[\text{O III}] \lambda 5007$  and  $[\text{O I}] \lambda 6300$  lines.

BPT diagram is almost insensitive to reddening). We plot the BPT diagrams in Figs 23 and 24 using the following criteria.

*Kewley criteria.* Galaxies above this line are AGN. Kewley et al. (2001) used a combination of photoionization and stellar population synthesis models to place a theoretical upper limit

on the location of star-forming galaxies on the BPT diagram,  $\log\left(\frac{[\text{O III}]}{\text{H}\beta}\right) = 0.61/\log([\text{N II}]/\text{H}\alpha) - 0.47 + 1.19$ .

*Kauffmann et al. (2003) criteria.* Galaxies below this line are purely star forming. Between Kewley and Kauffmann criteria is composite objects. Kauffmann et al. (2003) revised

Figure 19. A/N of the H $\beta$  lines.

the criteria as follows: a galaxy is defined to be an AGN if  $\log \left( \frac{[\text{OIII}]}{\text{H}\beta} \right) > 0.61/\log([\text{NII}]/\text{H}\alpha) - 0.05 + 1.3 \right)$ .

*LINERs–Seyfert line* (Schawinski et al. 2007). This line distinguishes LINERs from Seyfert galaxies  $\log \left( \frac{[\text{OIII}]}{\text{H}\beta} \right) = 1.05 \log \left( \frac{[\text{NII}]}{\text{H}\alpha} \right) + 0.45$ .

Sloan Digital Sky Survey (SDSS) emission-line galaxies occupy a well-defined region shaped like the wings of a seagull (Stasińska et al. 2008). Although the exact location of the line dividing the star-forming and AGN galaxies is still controversial (Kewley et al. 2001; Kauffmann et al. 2003; Stasińska et al. 2006).

All galaxies show important LINER emission, but that at least one has significant Seyfert emission areas, and at least one other has significant H II like emission line ratios for many pixels as shown

in Figs 23 and 24. This is in agreement with the long-slit data of these sources plotted on BPT diagrams in fig. 3 of McDonald et al. (2012).

However, there is a debate about the ionization mechanism in LINERs. The most viable excitation mechanisms are a low accretion-rate AGN (Kewley et al. 2006), photoionization by old pAGB stars (Stasińska et al. 2008) and fast shocks (Dopita & Sutherland 1995). Sarzi et al. (2010) investigate the ionizing sources for the gas in elliptical galaxies based on SAURON integral field spectroscopy whose spectra are limited to a relatively narrow wavelength range. They conclude that pAGB stars are the main source of ionization. In contrast, Annibali et al. (2010) analyse long-slit spectra of 65 ellipticals and claim that their nuclear line emission can be explained by excitation from the hard ionizing continuum from an

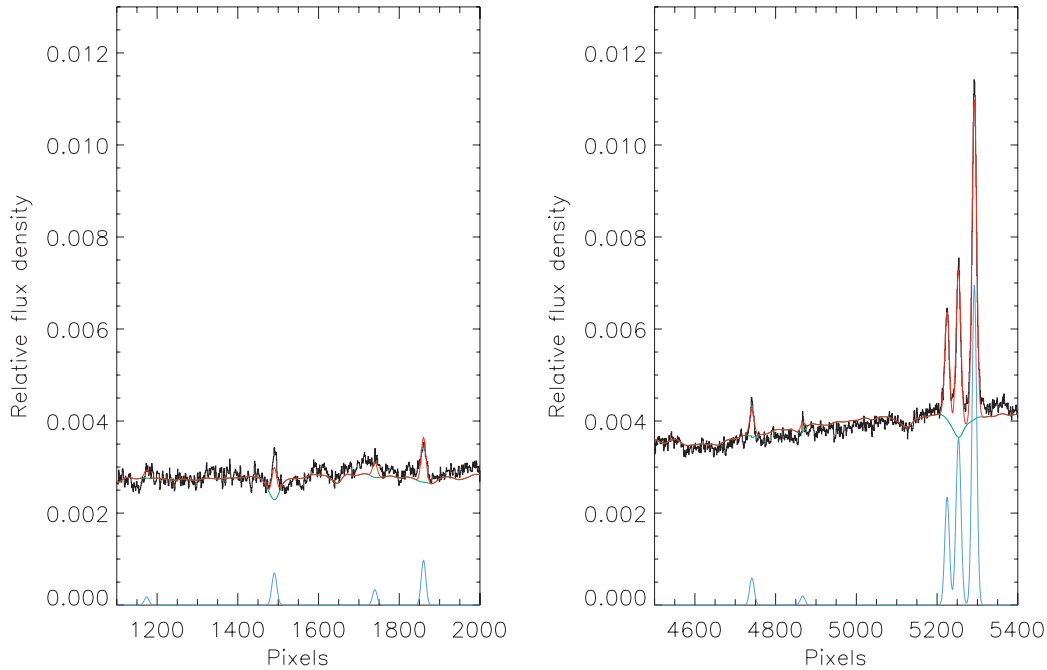


**Figure 20.** A random spectrum in the central region of MCG-02-12-039. The red line indicates the best-fitting stellar template and Gaussians at the emission lines, and the green line indicates the best-fitting stellar templates with the emission lines subtracted. The blue line indicates the relative flux for the measured emission lines. The lines are (from left to right) in the left-hand plot: [Ar IV], H $\beta$  and the [O III] doublet, and in the right-hand plot: [O I] doublet, [N II] doublet and H $\alpha$ . The H $\alpha$  A/N of this pixel was 15.

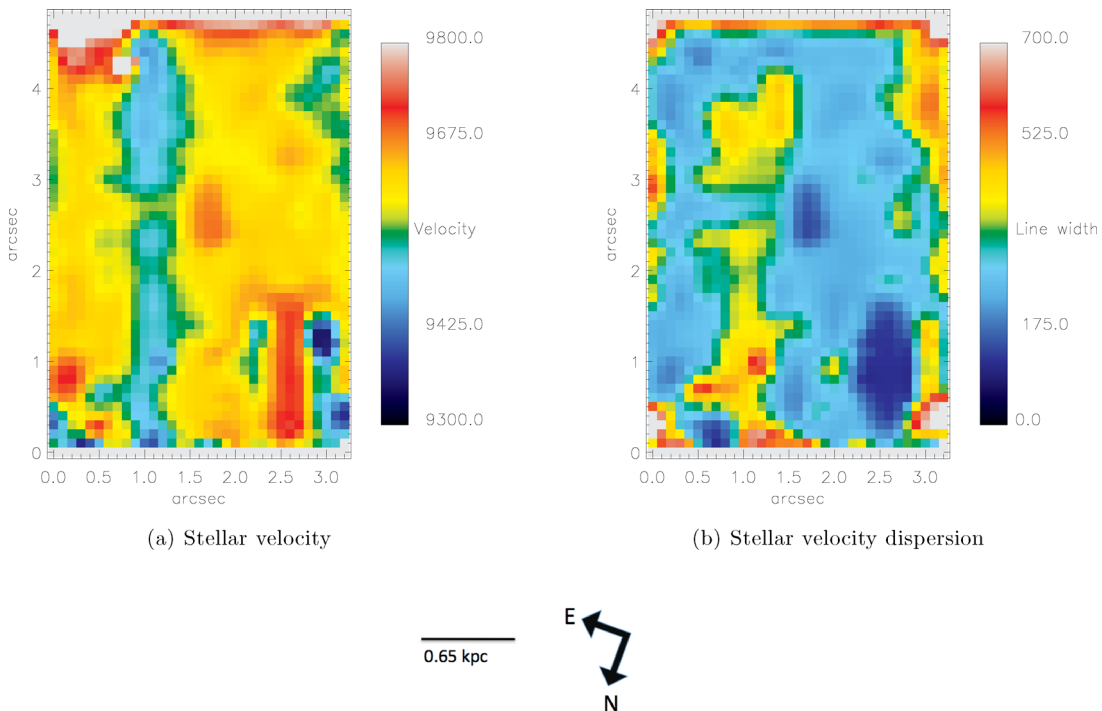


**Figure 21.** MCG-02-12-039: velocity and velocity dispersion of the absorption lines in  $\text{km s}^{-1}$ .

AGN and/or fast shocks. However, they cannot completely rule out a contribution from pAGB stars at large radii. Voit & Donahue (1997) suggested that sources of supplementary heating produce the LINER-like properties of the spectra, though not necessarily through the same mechanism in all systems.

Annibali et al. (2010) found that from the centre outward, galaxies move left and down in the BPT diagram for their study of 65 early-type galaxies. Thus, the hardness of the ionizing continuum decreases with galactocentric distance (up to half the half-light radius in the Annibali et al. 2010 sample). Figs 23 and 24 also

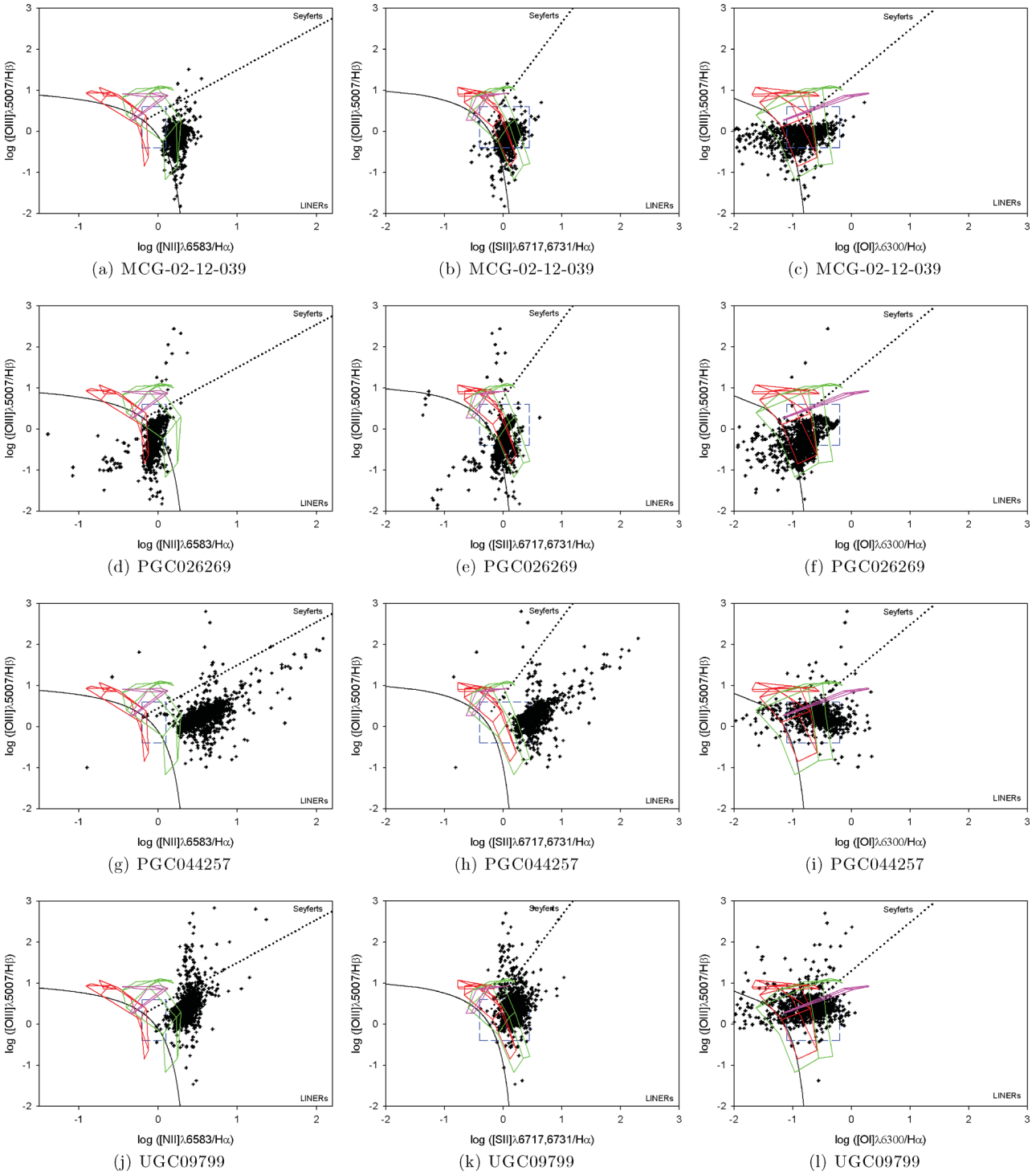


**Figure 22.** Diagnostic diagrams for all four galaxies. From left to right:  $\log([\text{O}\text{III}]\lambda 5007/\text{H}\beta)$  versus  $\log([\text{N}\text{II}]\lambda 6584/\text{H}\alpha)$ ,  $\log([\text{O}\text{III}]\lambda 5007/\text{H}\beta)$  versus  $\log([\text{S}\text{II}]\lambda\lambda 6731, 6717/\text{H}\alpha)$  and  $\log([\text{O}\text{III}]\lambda 5007/\text{H}\beta)$  versus  $\log([\text{O}\text{I}]\lambda 6300/\text{H}\alpha)$ . The black solid curve is the theoretical maximum starburst model from Kewley et al. (2001), devised to isolate objects whose emission line ratios can be accounted for by the photoionization by massive stars (below and to the left of the curve) from those where some other source of ionization is required. The black dashed curves in the  $[\text{S}\text{II}]\lambda\lambda 6731, 6717/\text{H}\alpha$  and  $[\text{O}\text{I}]\lambda 6300/\text{H}\alpha$  diagrams represent the Seyfert–LINER dividing line from Kewley et al. (2006) and transposed to the  $[\text{N}\text{II}]\lambda 6584/\text{H}\alpha$  diagram by Schawinski et al. (2007). The predictions of different ionization models for ionizing the gas are overplotted in each diagram. The boxes show the predictions of photoionization models by PAGB stars for  $Z = Z_\odot$  and a burst age of 13 Gyr (Binette et al. 1994). The purple lines represent the shock grids of Allen et al. (2008) with solar metallicity and pre-shock magnetic fields  $B = 1.0, 5.0$  and  $10 \mu\text{G}$  (left to right). The horizontal purple lines show models with increasing shock velocity  $V = 100, 500$  and  $1000 \text{ km s}^{-1}$ , and the densities  $n_e = 100 \text{ cm}^{-3}$ . Grids of photoionization by an AGN (Groves et al. 2004) are indicated by green and red curves, with  $n_e = 100 \text{ cm}^{-3}$  and a power-law spectral index of  $\alpha = -2, -1.4$  and  $-1.2$  (from left to right). The models for  $Z = Z_\odot$  (red) and  $Z = 2 Z_\odot$  (green), and the horizontal lines trace the ionization parameter  $\log U$ , which increases with the  $[\text{O}\text{III}]\lambda 5007/\text{H}\beta$  ratio from  $\log U = -3.6, -3.0, -2.0, -1.0$  and  $0.0$ .

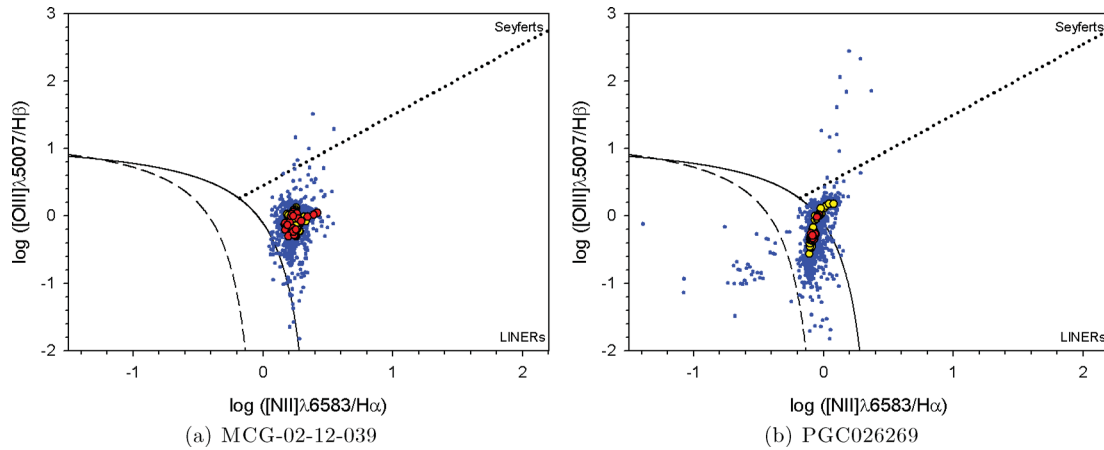


**Figure 23.** BPT diagram for MCG-02-12-039 and PGC 026269. The red circles indicate the central  $0.5 \times 0.5$  arcsec $^2$  of the galaxy, the yellow circles  $1.0 \times 1.0$  arcsec $^2$  and the blue circles the full  $3.5 \times 5.0$  arcsec $^2$ . The centre of the galaxy was determined as the luminosity peak in the continuum images in Fig. 1. The black solid curve is the theoretical maximum starburst model from Kewley et al. (2001), devised to isolate objects whose emission line ratios can be accounted for by the photoionization by massive stars (below and to the left of the curve) from those where some other source of ionization is required. The black dotted curve in the diagram represents the Seyfert–LINER dividing line from Kewley et al. (2006) and transposed to the [N II]  $\lambda 6584/\text{H}\alpha$  diagram by Schawinski et al. (2007).

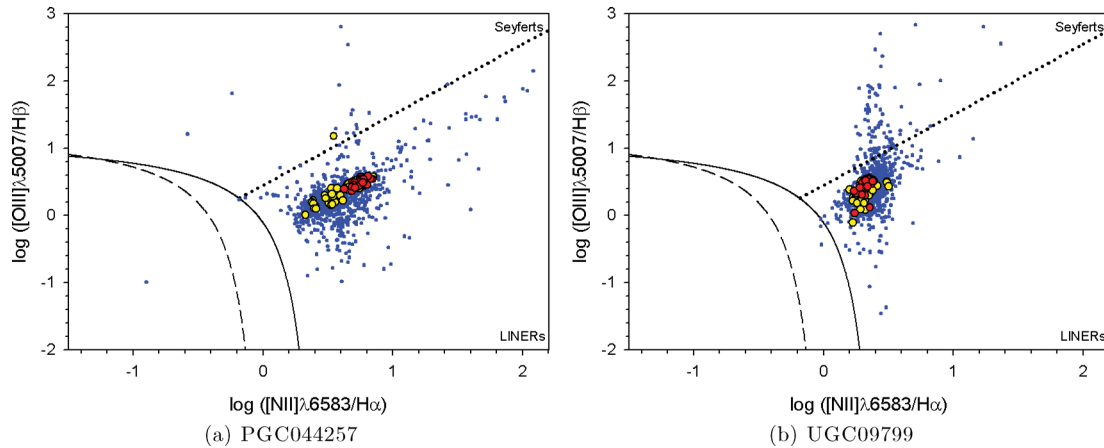


**Figure 24.** BPT diagram for PGC 044257 and UGC 09799. The red circles indicate the central  $0.5 \times 0.5$  arcsec $^2$  of the galaxy, the yellow circles  $1.0 \times 1.0$  arcsec $^2$  and the blue circles the full  $3.5 \times 5.0$  arcsec $^2$ . See caption of Fig. 23.

show the flux ratios as function of distance from the galaxy centre. The red circles indicate the central  $0.5 \times 0.5$  arcsec $^2$  of the galaxy, the yellow circles  $1.0 \times 1.0$  arcsec $^2$  and the blue circles the full  $3.5 \times 5.0$  arcsec $^2$ . The centre of the galaxy was determined as the luminosity peak in the continuum images in Fig. 1. In our case, the hardness of the ionizing continuum stay mostly uniform with galactocentric distance over out limited spatial extend. PGC 044257 shows an interesting core separation of the emission in the very centre of the galaxy in Fig. 24(a).

There is also the debate about which galaxies are LINERs (AGN) and which have just LINER-like emission (non-AGN). The division is usually made by looking at the extend of the LINER signature: core-dominated mean true LINER and diffuse means LINER like. The arising problem is that the scale of the SDSS fibres is already too large to make the distinction for most galaxies. For the nearby galaxies, the centroiding of the fibres is not accurate enough to be sure if the measured spectra cover the core of the galaxy. We have core-dominated LINER emission for at least three out of the four galaxies. Additional confirmation comes from the fact that at least one of our galaxies (PGC 026269) is a strong radio source (AGN, see Table 2). Similarly, our findings for UGC 09799 agree with Ed-

wards et al. (2009) who found line ratios consistent with Seyfert or LINER activity in most of their central spaxels for UGC 09799. Edwards et al. (2009) also found that the Seyfert signature dominated the central spaxels of the CCG (UGC 09799). The H $\alpha$  emission surrounding the BCG in this cluster is coincident with radio-blown bubbles in the central region of the cluster. These bubbles to the north and south of the cluster core are filled with radio emission, which likely originated from the AGN within the CCG (Blanton et al. 2003). Since the H $\alpha$  emission seen by McDonald et al. (2010) is primarily along the edges of the northern bubble, they suspect that shocks may be responsible for the heating in this case. However, for PGC 044257, McDonald et al. (2010) find very little evidence for an AGN in the cluster hosting the galaxy, in terms of the radio power, X-ray morphology and hard X-ray flux. Two of the galaxies in the current study have detected X-ray point sources in the CCG (PGC 026269 and UGC 09799) with large cavities in their X-ray haloes, suggesting that the AGN is influencing the surrounding medium.

We investigate this further by plotting the other BPT diagrams, on a spaxel-by-spaxel basis, for all four galaxies (shown in Fig. 24): [O III]  $\lambda 5007/\text{H}\beta$  versus [N II]  $\lambda 6584/\text{H}\alpha$ , [O III]  $\lambda 5007/\text{H}\beta$  versus

$[\text{S II}] \lambda\lambda 6717, 6731/\text{H}\alpha$  and  $[\text{O III}] \lambda 5007/\text{H}\beta$  versus  $[\text{O I}] \lambda 6300/\text{H}\alpha$ . One BCG PGC 026269 show several  $\text{H II}$  pixels in all three BPT diagrams. Fig. 23 shows that these  $\text{H II}$  pixels occur throughout the centre of the galaxy.

On these plots, we compare our observations to the photoionization models for pAGB stars with  $Z = Z_{\odot}$  (Binette et al. 1994). These models are consistent with most of our observations. A model with  $Z = 1/3 Z_{\odot}$  will be shifted towards lower values on the  $x$ -axis of the three BPTs. The pAGB scenario has recently been revisited by Stasinska et al. (2008), whose extensive grid of photoionization models (see their fig. 5) covers most of the regions occupied by our spatially resolved measurements.

Three other grids of ionization models are overplotted on the BPT diagrams (Fig. 24). The plotted AGN photoionization models (Groves, Dopita & Sutherland 2004) have an electron density,  $n_e = 100 \text{ cm}^{-3}$ , metallicities of solar,  $Z = Z_{\odot}$  (red grids), and twice solar (green grids), a range of ionization parameter ( $-3.6 < \log U < 0.0$ ) and a power-law ionizing spectrum with spectral index  $\alpha = -2, -1.4$  and  $-1.2$ . A harder ionizing continuum, with  $\alpha = -1.2$ , boosts  $[\text{S II}] \lambda\lambda 6717, 6731$  and  $[\text{O I}] \lambda 6300$  relative to  $\text{H}\alpha$ .

We also compared our results with shock models (Allen et al. 2008, purple grids). In Fig. 24, we plot the grids with  $Z = Z_{\odot}$ , pre-shock densities of  $100 \text{ cm}^{-3}$ , shock velocities of 100, 500 and  $1000 \text{ km s}^{-1}$  and pre-shock magnetic fields of  $B = 1, 5$  and  $10 \mu\text{G}$ . Shock models with a range of magnetic field strengths ( $B = 1, 5$  and  $10 \mu\text{G}$ ) match our observations. Interstellar magnetic fields of  $B \sim 1-10 \mu\text{G}$  are typical of what is observed in elliptical galaxies (Mathews & Brighenti 1997). Overall, shock models reproduce the majority of our data in the three emission-line ratio diagrams. The shock grids with lower metallicity [e.g. Large Magellanic Cloud (LMC) and Small Magellanic Cloud (SMC) metallicities] are not consistent with our measurements.<sup>3</sup>

As shown in Table 2 – we have very weak as well as strong radio fluxes in our small sample. We therefore believe that we are not particularly prone to biases such as the fact that a priori choice of galaxies with strong radio fluxes will result in finding a sample where high  $[\text{N II}]/\text{H}\alpha$  would be more common than in an optically or  $\text{H}\alpha$  selected sample only – where star forming high  $\text{H}\alpha/[\text{N II}]$  sources might be more abundant.

## 7 CONCLUSION

We present detailed IFU observations of the central few kiloparsecs of the ionized nebulae surrounding four active CCGs in cooling flow clusters (Abell 0496, 0780, 1644 and 2052). Our sample consists of CCGs with  $\text{H}\alpha$  filaments. We observed the detailed optical emission-line (and simultaneous absorption line) data over a broad wavelength range to probe the dominant ionization processes, excitation sources, morphology and kinematics of the hot gas (as well as the morphology and kinematics of the stars). Two of the four sources have not been observed with IFU data before (Abell 0780 and 1644), and for the other two sources we observed with significantly improved integration times (and number of lines) than previous studies (Hatch et al. 2007; Edwards et al. 2009). This will help form a complete view of the different phases (hot gas and stars) and how they interact in the processes of star formation and feedback detected in central galaxies in cooling flow clusters, as well as the influence of the host cluster.

<sup>3</sup> We downloaded the shock and AGN grids from the web page <http://www.strw.leidenuniv.nl/~brent/itera.html>

The total extinction maps are presented in Fig. 2 and show extinction which agrees well with previously derived long-slit values (where available). From long-slit spectra, Crawford et al. (1999) derived the total extinction of PGC 044257 as 0.46–0.63 mag. This agrees with the extinction we derived for the very centre of the galaxy in Fig. 2, but on average our spatially resolved extinction is slightly lower (0.195 mag). Crawford et al. (1999) derived an integrated internal extinction of  $E(B - V)_{\text{internal}}$  of 0.22 mag for the centre of UGC 09799. This corresponds very well to what we derived and plotted in Fig. 2, although we find that some regions show much higher internal extinction (on average 0.42 mag).

We derive a range of different kinematic properties, given the small sample size. For Abell 0496 and 0780, we find that the stars and gas are kinematically decoupled, and in the case of Abell 1644 we find that these components are aligned. For Abell 2052, we find that the gaseous components show rotation even though no rotation is apparent in the stellar components. To the degree that our spatial resolution reveals, it appears that all the optical forbidden and hydrogen recombination lines originate in the same gas for all the galaxies.

All galaxies show important LINER emission, but that at least one has significant Seyfert emission areas, and at least one other has significant  $\text{H II}$ -like emission-line ratios for many pixels (consistent with the long-slit observations of McDonald et al. 2012). We also show that the hardness of the ionizing continuum does not decrease with galactocentric distance (except for PGC 044257 that shows an interesting core separation of the emission in the very centre of the galaxy in Fig. 24a). The radial profiles of diagnostic line ratios,  $[\text{O III}] \lambda 5007/\text{H}\beta$  and  $[\text{N II}] \lambda 6584/\text{H}\alpha$ , show that they are roughly constant with radius for three of the four galaxies (all except PGC 044257). This indicates that the dominant ionizing source is not confined to the nuclear region in the two objects and that the ionized gas properties are homogeneous in the emission-line regions across each galaxy.

Overall, it remains difficult to disentangle the dominant photoionization mechanisms, even with more line measurements. The AGN photoionization models (with higher metallicity) are the best able to reproduce our spatially resolved line ratios in all of the three BPT diagrams simultaneously of most objects, even though shock models and pAGB stars cannot be conclusively eliminated. We also do not see extended  $[\text{O I}] \lambda 6300$  emission, following the morphology of the strong emission lines (e.g. Farage et al. 2010), therefore, it is unlikely that shock excitation is the dominant ionizing source in the galaxies of this limited sample. In addition, multiwavelength observations (as discussed in the previous section) favour the AGN photoionization mechanism, especially in the case of PGC 026269 and UGC 09799.

## ACKNOWLEDGEMENTS

SIL is financially supported by the South African National Research Foundation. We thank James Turner, Bryan Miller and Michele Cappellari for providing helpful scripts, as well as Marc Sarzi for helpful discussions. Based on observations obtained on the Gemini South telescope. The Gemini Observatory is operated by the Association of Universities for Research in Astronomy, Inc., under cooperative agreement with the NSF on behalf of the Gemini Partnership: the National Science Foundation (USA), the Science and Technology Facilities Council (UK), the National Research Council (Canada), CONICYT (Chile), the Australian Research Council (Australia), CNPq (Brazil) and CONICET (Argentina). This research has made use of the NASA/IPAC Extragalactic

Database (NED) which is operated by the Jet Propulsion Laboratory, California Institute of Technology.

## REFERENCES

- Allen M. G., Groves B. A., Dopita M. A., Sutherland R. S., Kewley L. J., 2008, ApJS, 178, 20
- Annibali F., Bressan A., Rampazzo R., Zeilinger W. W., Vega O., Panuzzo P., 2010, A&A, 519, 40
- Athanassoula E., Garioj A., García-Gómez C., 2001, MNRAS, 321, 353
- Baldwin J. A., Phillips M. M., Terlevich R., 1981, PASP, 93, 5 (BPT)
- Bildfell C., Hoekstra H., Babul A., Mahdavi A., 2008, MNRAS, 389, 1637
- Binette L., Raga A. C., Calvet N., Canto J., 1990, PASP, 102, 723
- Binette L., Magris C. G., Stasińska G., Bruzual A. G., 1994, A&A, 292, 13
- Blanton E. L., Sarazin C. L., McNamara B. R., 2003, ApJ, 585, 227
- Bohringer H. et al., 2001, A&A, 365, 181
- Brough S., Tran K.-V., Sharp R. G., Von der Linden A., Couch W. J., 2011, MNRAS, 414, L80
- Calzetti D., Armus L., Bohlin R. C., Kinney A. L., Koornneef J., Storchi-Bergmann T., 2000, ApJ, 533, 682
- Cappellari M., Emsellem E., 2004, PASP, 116, 138
- Cardelli J. A., Clayton G. C., Mathis J. S., 1989, ApJ, 345, 245
- Cardiel N., Gorgas J., Aragón-Salamanca A., 1998, MNRAS, 298, 977
- Crawford C. S., Allen S. W., Ebeling H., Edge A. C., Fabian A. C., 1999, MNRAS, 306, 857
- Crawford C. S., Hatch N. A., Fabian A. C., Sanders J. S., 2005, MNRAS, 363, 216
- De Lucia G., Blaizot J., 2007, MNRAS, 375, 2
- Dopita M. A., Sutherland R. S., 1995, ApJ, 455, 468
- Edge A. C., Stewart G. C., Fabian A. C., 1992, MNRAS, 258, 177
- Edwards L. O. V., Hudson M. J., Balogh M. L., Smith R. J., 2007, MNRAS, 379, 100
- Edwards L. O. V., Robert C., Mollá M., McGee S. L., 2009, MNRAS, 396, 1953
- Fabian A. C., Nulsen P. E. J., Steward G. C., Ku W. H.-M., Malin D. F., Mushotzky R. F., 1981, MNRAS, 196, 35
- Farage C. L., McGregor P. J., Dopita M. A., Bicknell G. V., 2010, ApJ, 724, 267
- Ferland G. J., Fabian A. C., Hatch N. A., Johnstone R. M., Porter R. L., van Hoof P. A. M., Williams R. J. R., 2009, MNRAS, 392, 1475
- Fisher D., Illingworth G., Franx M., 1995, ApJ, 438, 539
- Gaskell C. M., Ferland G. J., 1984, PASP, 96, 393
- Gerssen J., Allington-Smith J., Miller B. W., Turner J. E. H., Walker A., 2006, MNRAS, 365, 29
- Groves B. A., Dopita M. A., Sutherland R. S., 2004, ApJS, 153, 9
- Hamer S. L., Edge A. C., Swinbank A. M., Wilman R. J., Russell H. R., Fabian A. C., Sanders J. S., Salomé P., 2012, MNRAS, 421, 3409
- Hatch N. A., Crawford C. S., Fabian A. C., 2007, MNRAS, 380, 33
- Hicks A. K., Mushotzky R., 2005, ApJ, 635, 9
- Hu E. M., Cowie L. L., Wang Z., 1985, ApJS, 59, 447
- Johnson R. E., Markevitch M., Wegner G. A., Jones C., Forman W. R., 2010, ApJ, 710, 1776
- Jordán A., Côté P., West M. J., Marzke R. O., Minniti D., Rejkuba M., 2004, AJ, 127, 24
- Kauffmann G. et al., 2003, MNRAS, 341, 33
- Kewley L. J., Dopita M. A., Sutherland R. S., Heisler C. A., Trevena J., 2001, ApJ, 556, 121
- Kewley L. J., Groves B., Kauffmann G., Heckman T., 2006, MNRAS, 372, 961
- Laine S., Van der Marel R. P., Lauer T. R., Postman M., O'Dea C. P., Owen F. N., 2003, AJ, 125, 478
- Loubser S. I., Sánchez-Blázquez P., 2012, MNRAS, 425, 841
- Loubser S. I., Sansom A. E., Sánchez-Blázquez P., Soechting I. K., Bromage G., 2008, MNRAS, 391, 1009 (Paper I)
- Loubser S. I., Sánchez-Blázquez P., Sansom A. E., Soechting I. K., 2009, MNRAS, 398, 133
- McCarthy I. G. et al., 2010, MNRAS, 406, 822
- McDonald M., Veilleux S., Rupke D. S. N., Mushotzky R., 2010, ApJ, 721, 1262
- McDonald M., Veilleux S., Rupke D. S. N., Mushotzky R., Reynolds C., 2011, ApJ, 734, 95
- McDonald M., Veilleux S., Rupke D. S. N., 2012, ApJ, 746, 153
- McNamara B. R., O'Connell R. W., 1992, ApJ, 393, 579
- McNamara B. R., Wise M., Sarazin C. L., Jannuzi B. T., Elston R., 1996, ApJ, 466, L9
- McNamara B. R. et al., 2006, ApJ, 648, 164
- Marković T., Owen F. N., Eilik J. A., 2004, in Reiprich T., Kempner J., Soker N., eds, Proceedings of The Riddle of Cooling Flows in Galaxies and Clusters of Galaxies. Charlottesville, p. 61
- Mathews W. G., Brighenti F., 1997, in Arnaboldi M., Da Costa G. S., Saha P., eds, ASP Conf. Ser. Vol. 116, The Nature of Elliptical Galaxies. Astron. Soc. Pac., San Francisco, p. 396
- O'Dea C. P. et al., 2008, ApJ, 681, 1035
- Osterbrock D. E., 1989, Astrophysics of Gaseous Nebulae and Active Galactic Nuclei. University Science Books, Mill Valley, CA
- Osterbrock D. E., Ferland G. J., 2006, Astrophysics of Gaseous Nebulae and Active Galactic Nuclei. University Science Books, Sausalito, CA
- Peres C. B., Fabian A. C., Edge A. C., Allen S. W., Johnstone R. M., White D. A., 1998, MNRAS, 298, 416
- Peterson J. R., Kahn S. M., Paerels F. B. S., Kaastra J. S., Tamura T., Bleeker J. A. M., Ferrigno C., Jernigan J. G., 2003, ApJ, 590, 207
- Pipino A., Kaviraj S., Bildfell C., Hoekstra H., Babul A., Silk J., 2009, MNRAS, 395, 462
- Romeo A. D., Napolitano N. R., Covone G., Sommer-Larsen J., Antonuccio-Delogu V., Capaccioli M., 2008, MNRAS, 389, 13
- Salomé P., Combes F., 2003, A&A, 412, 657
- Sánchez-Blázquez P. et al., 2006, MNRAS, 371, 703
- Sarzi M. et al., 2006, MNRAS, 366, 1151
- Sarzi M. et al., 2010, MNRAS, 402, 2187
- Schawinski K. et al., 2007, MNRAS, 382, 1415
- Schlegel D. J., Finkbeiner D. P., Davis M., 1998, ApJ, 500, 525
- Stasińska G., Cid Fernandes R., Mateus A., Sodré L., Jr, Asari N. V., 2006, MNRAS, 371, 972
- Stasińska G., Vale Asari N., Cid Fernandes R., Gomez J. M., Schlickmann M., Mateus A., Schoenel W., Sodré L., Jr, 2008, MNRAS, 391, 29
- Tamura T., Bleeker J. A. M., Kaastra J. S., Ferrigno C., Molendi S., 2001, A&A, 379, 107
- van Dokkum P. G., 2001, PASP, 113, 1420
- Venturi T., Dallacasa D., Stefanachi F., 2004, A&A, 422, 515
- Voit G. M., Donahue M., 1997, ApJ, 486, 242
- Voit G. M., Cavagnolo K. M., Donahue M., Rafferty D. A., McNamara B. R., Nulsen P. E. J., 2008, ApJ, 681, 5
- Von der Linden A., Best P. N., Kauffmann G., White S. D. M., 2007, MNRAS, 379, 867
- White D. A., Jones C., Forman W., 1997, MNRAS, 292, 419
- Wilman R. J., Edge A. C., Swinbank A. M., 2006, MNRAS, 371, 93
- Wise M. W., McNamara B. R., Nulsen P. E. J., Houck J. C., David L. P., 2007, ApJ, 659, 1153

## APPENDIX A: STELLAR KINEMATICS COMPARISON

For comparison purposes, the kinematics were extracted from the IFU image along the same slit position as the long-slit data in Paper I. This comparison is showed in Figs A1–A3, and the data points compare satisfactory. We emphasize that the long-slit data were binned to a constant (higher) S/N, where the IFU data are three binned spaxels (0.3 arcsec) along the same alignment.

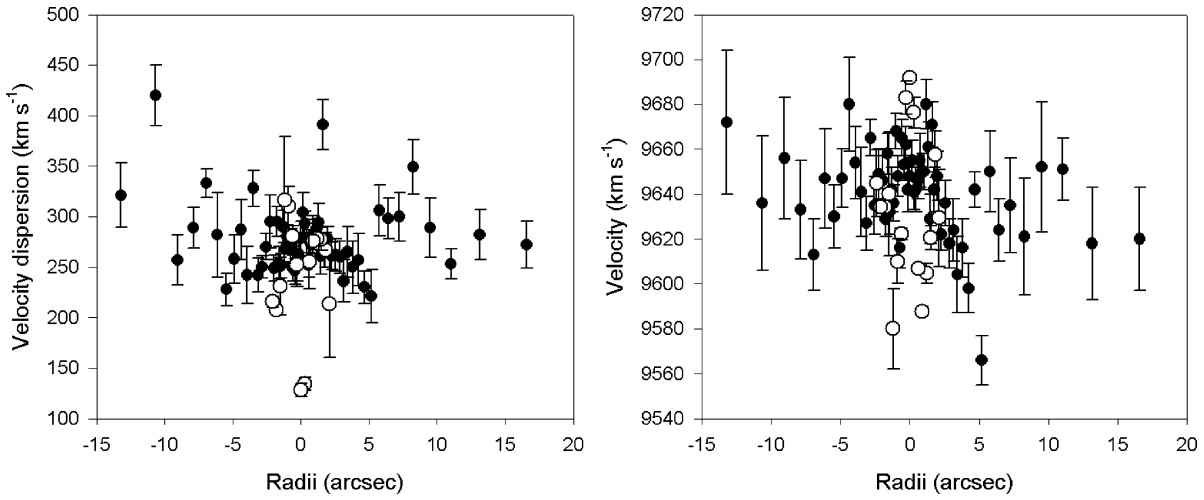


**Figure A1.** MCG-02-12-039: kinematic data (velocity and velocity dispersion) extracted from the IFU data (empty symbols), compared with long-slit data along the same axis from Paper I.

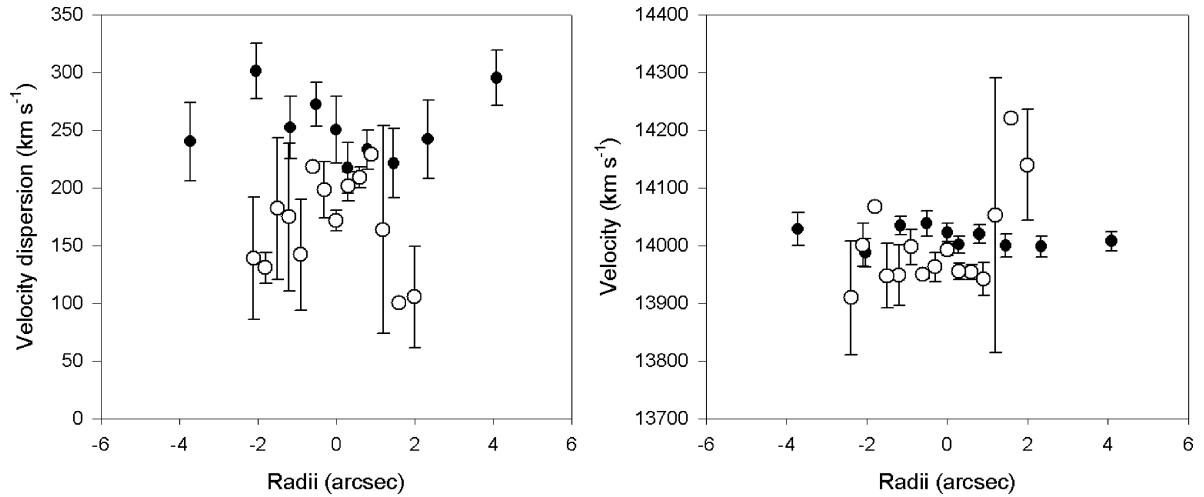


**Figure A2.** PGC 026269: kinematic data (velocity and velocity dispersion) extracted from the IFU data (empty symbols), compared with long-slit data along the same axis from Paper I.

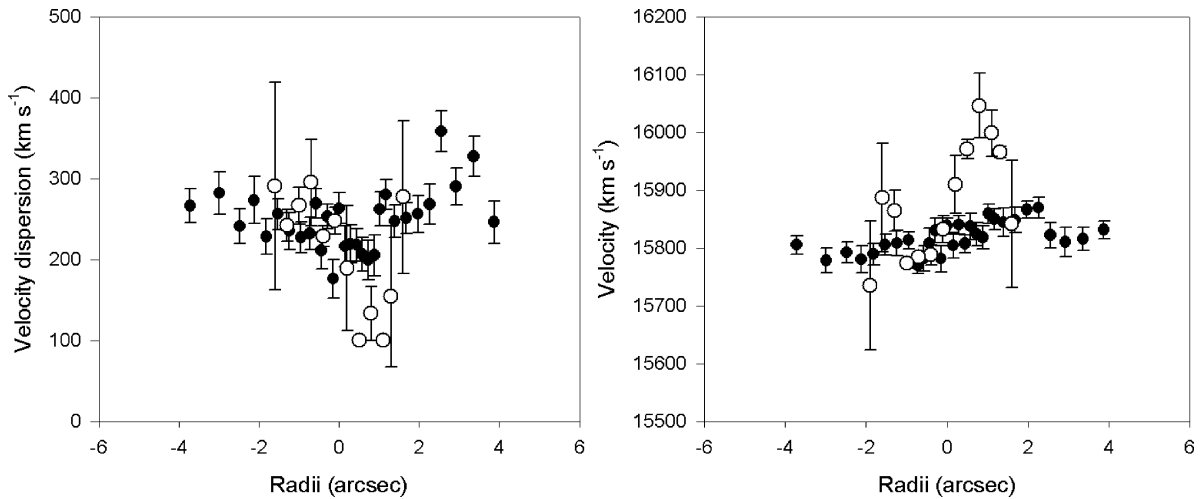


**Figure A3.** PGC 044257: kinematic data (velocity and velocity dispersion) extracted from the IFU data (empty symbols), compared with long-slit data along the same axis from Paper I.

## APPENDIX B: LINE MAPS

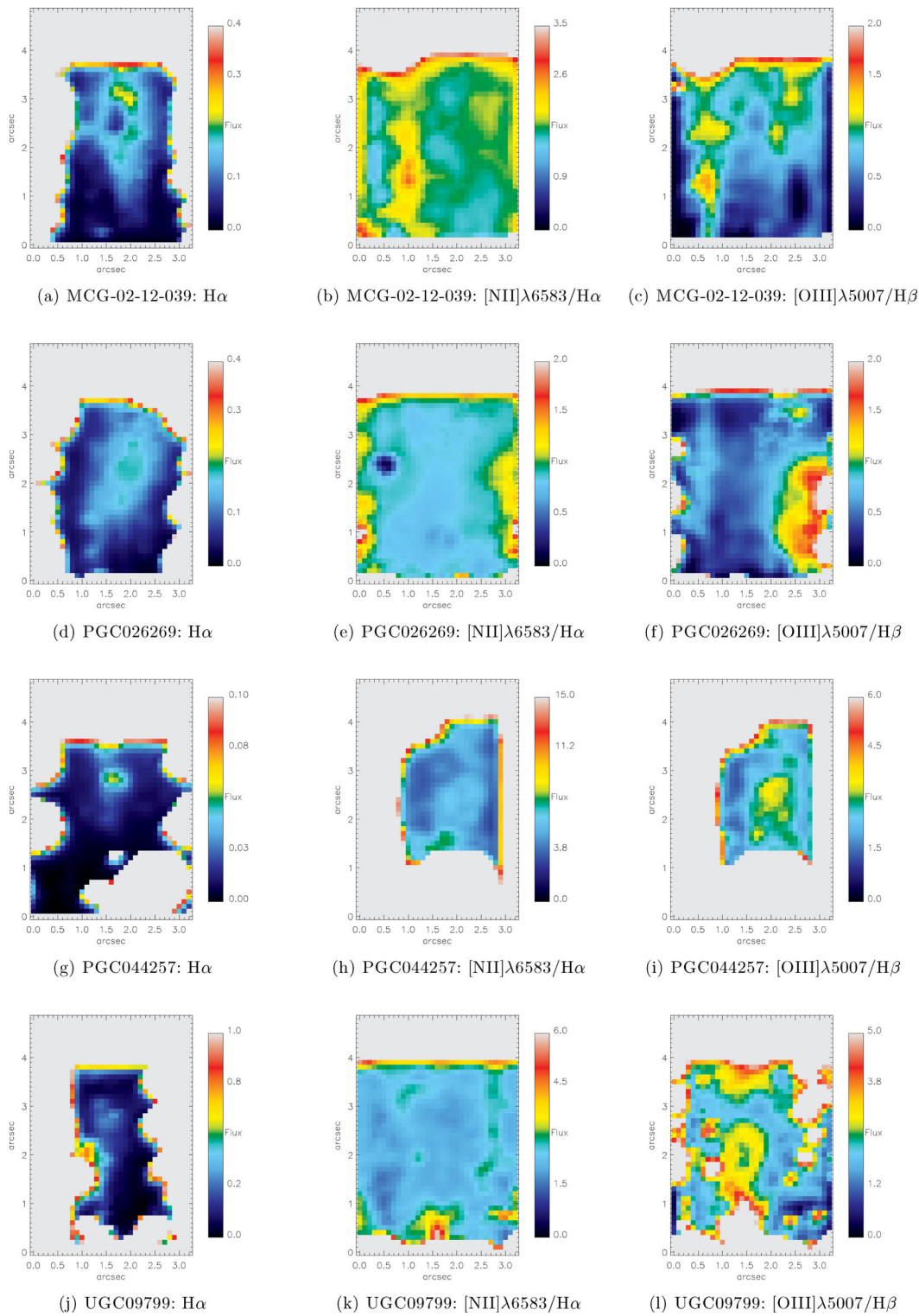


**Figure B1.** Absorption extracted, dereddened H $\alpha$ , [N II] $\lambda 6583/\text{H}\alpha$  and [O III] $\lambda 5007/\text{H}\beta$  emission maps in units of  $10^{-15} \text{ erg cm}^{-2} \text{ s}^{-1}$ .